



1 **Turbulence-permitting air pollution simulation for the** 2 **Stuttgart metropolitan area**

3 Thomas Schwitalla^{*1}, Hans-Stefan Bauer¹, Kirsten Warrach-Sagi¹, Thomas Bönisch², Volker
4 Wulfmeyer¹

5 ¹ Institute of Physics and Meteorology, University of Hohenheim, Garbenstrasse 30, 70599 Stuttgart, Germany.

6 ² High-Performance Computing Center Stuttgart (HLRS), Nobelstrasse 19, 70569 Stuttgart, Germany

7
8 *Correspondence to:* Thomas Schwitalla (thomas.schwitalla@uni-hohenheim.de)

9
10 **Abstract.** Air pollution is one of the major challenges in urban areas. It can have a major impact on human health
11 and society and is currently a subject of several litigations at European courts. Information on the level of air
12 pollution is based on near surface measurements, which are often irregularly distributed along the main traffic
13 roads and provide almost no information about the residential areas and office districts in the cities. To further
14 enhance the process understanding and give scientific support to decision makers, we developed a prototype for
15 an air quality forecasting system (AQFS) within the EU demonstration project “Open Forecast”.

16 For AQFS, the Weather Research and Forecasting model together with its coupled chemistry component (WRF-
17 Chem) is applied for the Stuttgart metropolitan area in Germany. Three model domains from 1.25 km down to a
18 turbulence permitting resolution of 50 m were used and a single layer urban canopy model was active in all
19 domains. As demonstration case study the 21 January 2019 was selected which was a heavy polluted day with
20 observed PM₁₀ concentrations exceeding 50 µg m⁻³.

21 Our results show that the model is capable to reasonably simulate the diurnal cycle of surface fluxes and 2-m
22 temperatures as well as evolution of the stable and shallow boundary layer typically occurring in wintertime in
23 Stuttgart. The simulated fields of particulates with a diameter of less than 10 µm (PM₁₀) and Nitrogen dioxide
24 (NO₂) allow a clear statement about the most heavily polluted areas apart from the irregularly distributed
25 measurement sites. Together with information about the vertical distribution of PM₁₀ and NO₂ from the model,
26 AQFS will serve as a valuable tool for air quality forecast and has the potential of being applied to other cities
27 around the world.

28 **1. Introduction**

29 Currently more than 50 % of the global population live in cities whereas the United Nations (UN) expect a further
30 increase by about 10 % in 2030 (UN, 2018). The UN also expect that in 2030 34% of the world population will
31 reside in cities with more than 500 000 inhabitants.

32 To protect human life, the World Health Organization (WHO) proposed maximum permissible pollution levels
33 (Maynard et al., 2017 and references therein). E.g. for particulate matter with particle diameters less than 10 µm
34 (PM₁₀), the critical value is an annual mean concentration of 20 µg m⁻³ or a daily mean value of 50 µg m⁻³ (WHO,
35 2005). For Nitrogen dioxide (NO₂) the critical values are 200 µg m⁻³ and 40 µg m⁻³ as daily and annual mean
36 values, respectively.



37 Due to a strong increase of road traffic in major European cities (Thunis et al., 2017), these pollution levels are
38 often violated in larger cities. This can lead to health and environmental problems and is currently part of several
39 litigations e.g. at the German Federal Administrative Court dealing with possible driving bans for non low-
40 emission vehicles. The basis for these litigations are mostly few local observations which are unevenly distributed.
41 In combination with special meteorological conditions like winter time thermal inversion layers it can be
42 misleading to conclude about the overall air quality in the city. According to e.g. the German Federal Immission
43 Control Ordinance¹ it is sufficient that traffic related measurements are representative for a section of 100 m, but
44 this is not representative for the commercial and office districts in the cities that are suffering from traffic control
45 in case of fine dust alerts and residential areas. Namely in residential areas health protection action plans require
46 representative air quality measures.

47 Therefore it becomes important to apply a more scientifically valid approach by applying coupled atmospheric
48 and chemistry models to predict air quality. Regional and global atmospheric models like the Weather Research
49 and Forecasting (WRF) model (Skamarock et al., 2019), the Consortium for Small Scale modeling (COSMO;
50 Baldauf et al., 2011), the Icosahedric Nonhydrostatic model (ICON; Zängl et al., 2015), or the Regional Climate
51 Model system (RegCM4; Giorgi et al., 2012) are often used to force offline chemistry transport models like
52 CHIMERE (Mailler et al., 2017), LOTOS-EUROS (Manders et al., 2017), EUROpean Air Pollution Dispersion
53 (EURAD; Memmesheimer et al., 2004), and Model for OZone And Related chemical Tracers (MOZART)
54 (Brasseur et al., 1998; Horowitz et al., 2003).

55 Several studies showed that combining an atmospheric model with an online coupled chemistry component is a
56 suitable tool for air quality and pollution modeling in urban areas at the convection permitting (CP) resolution
57 (Fallmann et al., 2014; Kuik et al., 2016; Zhong et al., 2016; Kuik et al., 2018; Huszar et al., 2020).

58 Compared to chemical transport models, coupled models like WRF-Chem (Grell et al., 2005), COSMO-ART
59 (Vogel et al., 2009), ICON-ART (Rieger et al., 2015), and the Integrated Forecasting System (IFS) MOZART
60 (Flemming et al., 2015) allow for a direct interaction of aerosols with radiation leading to a better representation
61 of the energy balance closure at the surface as it would be the case when applying an offline chemistry model.

62 As usually the terrain and land cover over urban areas show fine scale structures which are not resolved even by a
63 CP resolution, there is a need for turbulence permitting (TP) simulations with horizontal grid increments of a few
64 hundred meters or even less. Important features are, e.g., urban heat island effects (Fallmann et al., 2014; Fallmann
65 et al., 2016; García-Díez et al., 2016; Li et al., 2019) and local wind systems like mountain and valley winds due
66 to differential heating (Corsmeier et al., 2011; e.g. Jin et al., 2016). Also, micro- and mesoscale wind systems can
67 develop due to urban structures and the heterogeneity of the land surface. It is well known that TP simulations are
68 a promising tool to further enhance the understanding of processes in the atmospheric boundary layer (Heinze
69 et al., 2017b; Panosetti et al., 2016; Heinze et al., 2017a; Bauer et al., 2020) in urban areas (Nakayama et al., 2012;
70 Maronga et al., 2019; Maronga et al., 2020).

71 In order to further enhance the quality of the simulations, building and urban canopy models (UCM) are developed
72 (Martilli et al., 2002; Kusaka and Kimura, 2004; Salamanca and Martilli, 2010; Maronga et al., 2019; Scherer et
73 al., 2019; Teixeira et al., 2019). The main purpose of UCMs is to provide a better description of the lower

¹https://www.gesetze-im-internet.de/bimschv_39/anlage_3.html



74 boundaries over urban areas such as building, roof and road geometries and their interactions with atmospheric
75 water vapor, wind, and radiation.

76 With the EU-funded project Open Forecast (<https://open-forecast.eu/en/>) it was intended to develop a prototype
77 for an air quality forecasting system (AQFS) for the Stuttgart metropolitan area in southwest Germany. Open
78 Forecast is a demonstration project to show the potential of open data combined with supercomputer resources to
79 create new data products for European citizens and public authorities. The long-term goal is to provide end users
80 and political decision-makers a useful tool, particularly considering further urbanization, heat island effects as well
81 as potential driving restrictions due to recent EU decisions on emission limits.

82 For our AQFS we use the WRF-Chem NWP model (Grell et al., 2005; Skamarock et al., 2019) as the WRF model
83 is extensively evaluated over Europe at different time scales and horizontal resolutions (San José et al., 2013;
84 Warrach-Sagi et al., 2013; Milovac et al., 2016; Lian et al., 2018; Molnár et al., 2019; Bauer et al., 2020; Coppola
85 et al., 2020; Schwitalla et al., 2020). It can easily be set up in a nested configuration over all regions of the Earth.
86 Compared to PALM-4U model, the nested model domains are driven by the full atmospheric and chemical
87 information from the parent domain along its lateral boundaries. Also, it contains well-characterized combinations
88 of parameterizations of turbulence and cloud microphysics in the outer domain that are consistent with the inner
89 TP domains where the high-quality cloud parameterization remains. No switch between different model systems
90 is required, which is expected to provide a great advantage with respect to the skill of air pollution and
91 meteorological forecasts.

92 To enhance the forecast skill, suitable variational and ensemble-based data assimilation systems are already in
93 place to further improve the meteorological initial conditions (Barker et al., 2012; Zhang et al., 2014; Kawabata et
94 al., 2018; Thundathil et al., 2020) and the chemical initial conditions (Chen et al., 2019; Sun et al., 2020) but this
95 is beyond the scope of our study.

96 The Parallelized Large-Eddy Simulation Model (PALM) model (Maronga et al., 2015) is another widely used TP
97 simulation model over Europe. PALM did not include the full interaction between land-surface, radiation, cloud
98 microphysics and chemistry during the performance of our study. The very recent version 6.0 of PALM-4U
99 (PALM for urban applications) (Maronga et al., 2020) is expected to contain a fully coupled chemistry module
100 (Khan et al., 2020, under review).

101 Fallmann et al. (2016) and Kuik et al. (2016) performed air quality simulations with WRF-Chem over the cities of
102 Berlin and Stuttgart on a CP resolution down to 1km and less than 40 model levels. They used the TNO-MACC
103 emission inventory (Kuenen et al., 2014) which is available as an annual totals on a 7 km x 7 km resolution. As
104 the topography of Stuttgart is very complex, the AQFS applies the WRF-Chem model on a turbulence permitting
105 horizontal resolution using 100 model levels to account for the shallow boundary layer occurring during
106 wintertime. In addition, we applied a local emission data set from the Baden-Württemberg State Institute for the
107 Environment, Survey and Nature Conservation available as annual mean on a horizontal resolution of 500 m x 500
108 m to resolve fine-scale emission structures.

109 Our study focuses on the methodology how to set up a AQFS prototype by using WRF-Chem and its application
110 to a typical wintertime situation in the Stuttgart metropolitan area. The manuscript is set up as follows: section 2
111 describes the design of our AQFS model system on the turbulence permitting resolution of 50 m followed by a



112 description of the selected case study. Section 4 shows the results including a discussion, sect. 5 summarizes our
113 work and gives an outlook on potential future enhancements of the AQFS prototype.

114 2. AQFS design

115 2.1. WRF model set-up

116 For our AQFS, we selected the Advanced Research WRF-Chem model in version 4.0.3 (Grell et al., 2005;
117 Skamarock et al., 2019). To reach the targeted resolution of 50 m, three model domains have been applied with
118 horizontal resolutions of 1250 m, 250 m, and 50 m and encompasses 800*800 grid cells in the outer domain and
119 601*601 grid cells in the two inner TP domains. The reason to start with a resolution of 1250 m in the outermost
120 domain is to avoid the application of a convection parametrization which can deteriorate the model results (Prein
121 et al., 2015; Coppola et al., 2020). The areas of model domain 1 and 3 are shown in Fig. 1.

122 As seen from Fig. 1b, the Stuttgart metropolitan area is characterized by an elevation variation of more than 300
123 m. The lowest elevation is approx. 220 m in the basin while the highest elevation reaches up to 570 m. As the main
124 traffic roads are in the basin, especially during wintertime this often leads to a worsening of the air quality as the
125 surrounding prevents an air mass exchange due to the stationary temperature inversion.

126 For the WRF model system land cover and soil texture fields are not available at resolutions higher than 500m.
127 Therefore we reclassified land cover data from the Copernicus CLC 2012 data set (European Union, 2012),
128 available on a resolution of 100 m, from the original 44 categories to the categories applied in the WRF model for
129 the simulations of the outer 2 domains. For the innermost model domain, we incorporated the most recent high-
130 resolution land-cover data set from the Baden-Württemberg State Institute for the Environment (LUBW), which
131 is derived from Landsat (Butcher et al., 2019) in 2010 and is available at 30 m resolution ([https://udo.lubw.baden-
132 wuerttemberg.de/public/](https://udo.lubw.baden-wuerttemberg.de/public/)) This data set was also reclassified to the corresponding land cover categories used in
133 WRF and is shown in Fig. 2.

134 The resolution of the provided default Food and Agriculture Organization of the United Nations (FAO) soil texture
135 data is only 10 km, therefore we used soil texture data from the International Soil Reference and Information
136 Centre (ISRIC) SoilGrids project (Hengl et al., 2014; Hengl et al., 2015). These data are available on a resolution
137 of 250 m. Terrain information was provided by the National Center for Atmospheric Research (NCAR) derived
138 from the Global multi-resolution terrain elevation data 2010 (GMTED2010) data set (Danielson and Gesch, 2011)
139 for domain 1. As the horizontal resolution of the GMTED2010 data set is 1 km, the 3" gap-filled Shuttle Radar
140 Topography Mission (SRTM) data set (Farr et al., 2007) is used for domain 2. As this resolution is still too coarse
141 for our targeted resolution of 50 m, the Digital Elevation model Europe (EU-DEM; European Union, 2017),
142 available at a resolution of 25 m, is used for the innermost domain.

143 In our set-up, we use 100 vertical levels for all domains using the traditional terrain following coordinate system
144 in WRF; 20 of the levels are distributed in the lowest 1100 m above ground level (AGL). All domains apply the
145 Noah-MP land surface model (Niu et al., 2011; Yang et al., 2011), the revised MM5 surface layer scheme based
146 on Monin-Obukhov similarity theory (Jiménez et al., 2012), the Thompson 2-moment cloud microphysics scheme
147 (Thompson et al., 2008) and the Rapid Radiative Transfer Model for GCMs (RRTMG; Iacono et al., 2008) for
148 parametrizing longwave and shortwave radiation. Due to the coarser resolution of the outermost domain, we
149 applied the Yonsei University (YSU; Hong et al., 2006) planetary boundary layer (PBL) parametrization in D01



150 only. As suggested by the WRF user guide, we applied the sub-grid turbulent stress option for momentum
151 (Kosovic, 1997) in domains two and three. The complete namelist settings are provided in the supplement.

152 As the finest resolution applied for the AQFS is 50 m, the more sophisticated Building Effect Parameterization
153 (BEP; Martilli et al., 2002) is not applied. as this scheme does not work with our selection of parametrizations.
154 Instead, the single layer urban canopy model (UCM) (Kusaka and Kimura, 2004) is selected to improve the
155 representation of the urban canopy layer and the surface fluxes. The parameters needed by the UCM are read in
156 from the lookup table URBPARAM.TBL which was adjusted for the Stuttgart area following Fallmann (2014).

157 Atmospheric chemistry is parametrized by the Regional Acid Deposition Model 2nd generation (RADM2) model
158 (Stockwell et al., 1990). RADM2 features 63 chemical species including photolysis and more than reactions.
159 Aerosols are represented by the Modal Aerosol Dynamics Model for Europe (MADE) and Secondary Organic
160 Aerosol Model (SORGAM) scheme (Ackermann et al., 1998; Schell et al., 2001) considering size distributions,
161 nucleation, coagulation, and condensational growth. The combination of RADM2_MADE-SORGAM is a
162 computationally efficient approach and is widely used for simulations over Europe (Forkel et al., 2015; Mar et al.,
163 2016). To further enhance vertical mixing of CO to higher altitudes during nighttime over urban grid cells, the if-
164 statements in the dry deposition driver of WRF-Chem at lines 690 and 707 have been deleted according as shown
165 in the supplement of Kuik et al. (2018).

166 Due to the complexity of the chemistry model in combination with the very high horizontal resolution and the
167 calm meteorological conditions, the adaptive model time step option was chosen instead of a fixed time step.
168 Model output is available in 5 min intervals for the innermost model domain.

169 Our single day case study on the turbulence permitting (TP) scale is designed to serve as a test bed to set up an air
170 quality forecasting system prototype for the Stuttgart metropolitan area. For process studies, the model chain itself
171 can be applied to other areas over the globe as long as 1) detailed land cover and soil texture data are available,
172 2) high-resolution emission data not only from traffic are available. The new model system can be even applied in
173 a forecast and warning mode, if near real time emission data exist. As the computational demands of applying
174 WRF-Chem on the TP scale are very high, access to an HPC system is a prerequisite.

175 **2.2. Model initialization**

176 The meteorological initial and boundary conditions were provided by the operational ECMWF integrated
177 forecasting system (IFS) analysis on model levels. The IFS is a global model with 9 km horizontal resolution and
178 applies a sophisticated four-dimensional variational (4DVAR) data assimilation system (Bonavita et al., 2016).
179 The data have been retrieved from the ECMWF Meteorological Archival and Retrieval System (MARS) and were
180 interpolated to a resolution of 0.05°.

181 The initialization and provision of the boundary conditions of the chemistry of the model is done with data from
182 the Whole Atmosphere Community Climate Model (WACCM; Marsh et al., 2013) using the Model for Ozone and
183 Related Chemical Tracers (MOZART) conversion tool MOZBC (Pfister et al., 2011). As the resolution of
184 WACCM is very coarse, the input data was extended by the ECMWF Copernicus Atmosphere Monitoring Service
185 (CAMS) reanalysis data set on 60 model levels and 40 km horizontal resolution (Inness et al., 2019).

186 **2.3. Emission data**



187 The emission data set used in this study is a combination of three products. Global input data sets containing
188 coarse resolution emissions from different sources are obtained from the BRAMS numerical modeling system
189 (Freitas et al., 2017). The PREP-CHEM-SRC tool (Freitas et al., 2011) is then applied as pre-processor to convert
190 these emissions to the appropriate WRF units and interpolate the data onto the WRF model grid.

191 As global emission data sets have a very coarse resolution in space and time, higher resolution emission data for
192 Europe from the Copernicus Atmosphere Monitoring Service (CAMS; Copernicus) CAMS-REG-AP product
193 became available (Granier et al., 2019). Its resolution is approx. 7×7 km and it is based on total annual emissions
194 from 2016. This product provides emissions of PM_{10} , $PM_{2.5}$, SO_2 , CO, NO_x , and CH_4 and contains sources from
195 different sectors, separated into ten different categories following the Gridded Nomenclature For Reporting
196 (GNFR; Granier et al., 2019).

197 The third emission data set (BW-EMISS) deployed in our study was obtained from the Baden-Württemberg State
198 Institute for the Environment (LUBW). This data set contains annual mean emissions from different sectors
199 following the GNFR classification and is currently available only until 2014 and has a horizontal resolution of 500
200 m. Unfortunately, more recent quality-controlled data sets were not available when our study was performed. It is
201 expected that annual emissions for 2018 will become available by mid of 2021.

202 As CAMS-REG-AP and BW-EMISS only contain annual sums or annual mean values, a temporal decomposition
203 was applied for both data sets following Denier van der Gon et al. (2011). Depending on the GNFR code, the data
204 are first projected onto the corresponding month, followed by the corresponding day of the week and the hour of
205 the day. A similar approach was performed e.g. in Resler et al. (2020, under review) for the city of Prague. After
206 finishing the decomposition, the data are converted to the corresponding units and interpolated onto the WRF
207 model grid using the Earth System Model Framework (ESMF; Valcke et al., 2012) interpolation utilities.

208 Figure 3 shows an example of the NO_2 emissions derived from the CAMS-REG-AP product (left) and the emission
209 data derived from the LUBW data set (right) on January 21, 2019 at 07 UTC.

210 Due to its much higher horizontal resolution, the BW-EMISS data set (Fig. 3b) shows much more detailed
211 structures for the NO_2 emissions which are mainly caused by road traffic.

212 In addition, the following adjustments have been performed: 1) NO_x emissions from forest grid cells have been
213 reduced by 90 %, 2) Road traffic NO_x emissions were transformed into 90 % NO and 10 % NO_2 emissions
214 following Kuik et al. (2018) 3) All emissions from Stuttgart airport were reduced by 90 % during the nighttime
215 flight ban between 00 UTC and 04 UTC as well as after 21 UTC.

216 The WRF-Chem model only ingests one emission data set per species, hence emissions from the different GNFR
217 categories have been accumulated to a single emission data set before performing the simulation. Figure 4
218 summarizes all necessary steps and the complete data and workflow of the AQFS prototype.

219 **2.4. Observations**

220 We used data from three meteorological stations (Stuttgart-Schnarrenberg ($48.8281^\circ N$ $9.2^\circ E$, elevation 314 m),
221 Stuttgart Airport ($48.6883^\circ N$ $9.2235^\circ E$, elevation 375 m), and Institute of Physics and Meteorology (IPM) at the
222 University of Hohenheim ($48.716^\circ N$ $9.213^\circ E$, elevation 407 m) to validate the simulated 2-m temperatures; data



223 are available every 10 minutes. The locations are indicated by the black dots Fig. 1b. In addition, the radiosonde
224 data from Stuttgart-Schnarrenberg were used.

225 As the incorporated emissions are from 2014 and are based on annual values, it would be rather misleading to
226 compare the observed pollutant concentrations directly with the model output. For instance, the actual traffic, the
227 sequence of traffic lights and traffic congestions of this particular day cannot be realistically represented. In
228 addition, all diagnosed or prognostic chemical quantities are only available on model levels (with the lowest model
229 half level being at ~15 m above ground) so that simulated concentrations need to be interpolated to the
230 measurement heights at 2.5–3.5 m AGL. This extrapolation may cause even more uncertainty. Therefore we
231 decided not to use pollution measurements for model evaluation but we studied the results based on process
232 understanding and plausibility arguments.

233 3. Case study description

234 For our study, we selected 21 January 2019. This day was characterized as “fine dust alarm” situation (Stuttgart
235 Municipality and German Meteorological Service (DWD), 2019) which is defined by a combination of the
236 following criteria:

- 237 1. Expected daily maximum PM_{10} concentration at Stuttgart Neckartor (NT in Fig. 1b) is higher than $30 \mu\text{g}$
238 m^{-3}
- 239 2. No rain on the following day
- 240 3. 10-m wind speed less than 3 m s^{-1} from south to northwest directions ($180\text{--}330^\circ$)
- 241 4. Nocturnal atmospheric inversion
- 242 5. Mixing layer depth less than 500 m during the day
- 243 6. Daily average 10-m wind speed less than 3 m s^{-1} from all directions

244 A sufficient criterion is a higher PM_{10} concentration following (1). If (1) is not fulfilled, then (2) and (3) together
245 with either (4) and/or (5) must be fulfilled. If only (4) or (5) is fulfilled, then (6) must be considered. For our case
246 study, the criteria 1-5 were fulfilled.

247 Figure 5 shows the observed PM_{10} and NO_2 concentrations at several stations in our model domain. From Fig. 5a
248 the high NO_2 concentrations at Neckartor and Hohenheimer Strasse occurring after sunrise can be clearly
249 identified. While these measurements are taken next to main roads, the other stations show considerably lower
250 NO_2 concentrations throughout the day. The PM_{10} concentrations (Fig. 5b) show extremely high values at
251 Neckartor exceeding $100 \mu\text{g m}^{-3}$ around noon time and the evening rush hour which clearly meets the main criteria
252 of the “fine dust alarm situation”. The other stations, which are not directly taken near main roads with heavy
253 traffic show considerably lower PM_{10} concentrations around $40 \mu\text{g m}^{-3}$.

254 This day was a typical winter weather situation. Central Europe was located at the east flank of a blocking high
255 pressure system located over the East Atlantic together with moderate to low horizontal geopotential gradients and
256 resulting weak winds at 500 hPa in southwestern Germany (Fig. 6a).

257 Near surface temperatures are below freezing level, between 1000 and 850 hPa very light easterly winds
258 characterize the flow, and a dry layer is present around 925 hPa (Fig. 6b). Above 850 hPa, the wind direction
259 rapidly changes to westerly directions, but the wind speeds remain below 5 m s^{-1} (see Fig. 7a).



260 The inversion between the two air masses inhibits vertical mixing leading to higher concentrations of aerosols in
261 the lowest few hundred meters above ground (AGL) and preventing air mass exchange aloft. This inversion is
262 further enhanced by the special orography of Stuttgart city (see later Fig. 15).

263 4. Results and Discussion

264 4.1. Meteorological quantities

265 A Skew-T diagram of the observed and simulated temperature, dew point, and wind profiles allows to evaluate the
266 stratification conditions of the model. Figure 7a shows the vertical profile of the model initial conditions at
267 Stuttgart-Schnarrenberg valid at 00 UTC 21 January 2019 in comparison with the observations.

268 The initial conditions agree well with the sounding showing a weak temperature inversion around 900 hPa with
269 high relative humidity values up to 650 hPa. The observed and simulated lifting condensation level is 940 hPa and
270 the integrated water vapor (PWAT) is 8 mm. Wind speed and direction agree with the observations showing a
271 wind shear above 850 hPa associated with low wind speeds of less than 5 m s^{-1} .

272 To further evaluate the stratification conditions during the day, Figure 7b shows the observed and simulated
273 temperature, dew point, and wind profiles at 11 UTC. The vertical structure of the observation and the simulation
274 has an almost perfect agreement. The temperature inversion layer at 910 hPa is well captured although the
275 simulated temperatures below the inversion are too high by about 1.5 K. The humidity profile (expressed as
276 dewpoint profile) is also very well captured with the largest moisture content below 870 hPa. Wind speed and
277 direction above 850 hPa agree well with the observation throughout the atmosphere. In regard of the vertical model
278 resolution, the wind situation in the lowest 1000 m AGL is also reasonably represented.

279 Figure 8 exemplarily shows the simulated 2-m temperature together with 10-m wind velocities at 12 UTC (noon
280 time) to display the complexity of the Stuttgart metropolitan area.

281 The 2-m temperatures show a daytime warming of downtown Stuttgart and the Neckar Valley while still
282 temperature slightly below 0°C are present at higher elevations (blue colors in Fig. 8). The wind situation is very
283 complex due to weak wind speeds in combination with a shallow boundary layer (see later Fig. 16) but the wind
284 flow along the upper Neckar river (south of 48.75°) is strongly pronounced. After sunset, wind speed starts to
285 increase and the channeling effect along the Neckar weakens (not shown).

286 Figure 9 shows an evaluation of the diurnal cycle of 2-m temperatures at the three measurement sites
287 Schnarrenberg, IPM and airport. Sunrise is at 07 UTC and sunset at 16 UTC and the model data are averaged over
288 5 grid cells around the measurement site. The northern station Schnarrenberg shows a lower temperature
289 throughout the day than the other two stations, which are situated 3 km apart at a similar elevation. The temperature
290 is about 1 K colder during the day and 0.5 K colder during the night.

291 At Schnarrenberg, the observed diurnal cycle is reasonably well simulated with WRF. Between 00 and 15 UTC, a
292 warm temperature bias of 1 K is present in the simulation, which turns into a small negative bias after sunset. At
293 IPM, the simulation shows a cold bias until 04 UTC turning into a warm bias as the strong temperature drop is not
294 simulated until 06:30 UTC. After 09 UTC until sunset the simulated temperature agrees well with the observations
295 while later a cold bias of around 1 K is present.



296 For the airport station, the model stays too warm with a positive bias of almost 2 K between 05 and 09 UTC.
297 During the further course of the day, the bias reduces to 1 K at noon while after sunset it turns into a negative bias
298 of 1 K.

299 A possible reason for the larger differences at the airport and IPM before (after) sun rise (sun set) is the occurrence
300 of low stratus or fog. At the beginning of the simulation, cloud coverage were reported by 5–7 octas (broken
301 clouds) over Schnarrenberg and the airport at approx. 500 m AGL (not shown) while after 04 UTC the low level
302 clouds started to diminish at Schnarrenberg first leading to a strong cooling until the early morning which is seen
303 as a temperature drop in the observations shown in Fig. 9. This temperature drop at Schnarrenberg and IPM is also
304 simulated but with a delay of approx. 2 h. During the evening transition and the following night, the low stratus
305 is developing again at the measurement sites with a ceiling of 500 m AGL but is not simulated and thus contributes
306 to a stronger cooling in the model. Another contributing factor to the delayed cloud dissipation could be the
307 turbulence spin-up time (Kealy et al., 2019), but this is beyond the scope of this study.

308 Although no measurements of sensible heat and ground heat fluxes are available, diurnal cycles of the fluxes at
309 the three locations IPM, Schnarrenberg, and airport were investigated. Figure 10 shows the simulated surface
310 sensible heat and ground heat flux at the three different meteorological measurement sites.

311 The sensible heat flux (Fig. 10a) shows a typical diurnal cycle with fluxes around zero before (after) sunrise
312 (sunset). During the day, the model simulates typical wintertime sensible heat fluxes between 40 and 100 W/m²
313 (e.g. Zieliński et al., 2018), which nicely shows a dependency on the different underlying land cover types. Lower
314 sensible heat fluxes occur over the sparsely vegetated surface at the airport as compared to the cropland station
315 IPM. As the algorithm to diagnose the 2-m temperature in NOAHMP is rather complex, no clear correlation
316 between SH and the 2-m temperature shown in Fig. 9 can be made. The latent heat fluxes (not shown) are almost
317 zero at Schnarrenberg and less than 10 W m⁻² at the other two locations due to cold and dry winter conditions

318 The simulated ground heat flux (Fig. 10b) shows an interesting behavior. Until sunrise, the simulated GRDFLX at
319 the airport and IPM shows fluctuations around -50 W m⁻² indicating some low levels clouds in accordance with
320 the too high simulated 2-m temperatures shown in Fig. 9. During the further course of the day, IPM and airport
321 show a clear diurnal cycle with maximum values between 100 and 170 W m⁻² reflected in the highest surface
322 temperatures during the day (not shown).

323 At Schnarrenberg, most of the time the ground heat flux is less than zero indicating a cooling of the soil, while
324 between 12 UTC and 16 UTC small positive values are simulated. As Schnarrenberg is categorized as low
325 intensity residential (category 31) with an urban fraction of 0.5 and the UCM is applied here, energy is mainly
326 stored in the urban canopy layer instead of being transferred into the soil.

327 As this day was characterized by a shallow PBL and a temperature inversion, it is worth to investigate the PBL
328 evolution during the day. Figure 11 shows time-height cross sections of potential temperature at IPM (top) and
329 Schnarrenberg (bottom).

330 Both locations are characterized by a very stable shallow boundary layer until 09 UTC with a depth of less than
331 200 m. Between 03 and 09 UTC the temperatures at Schnarrenberg are up to 1.5 K colder near the surface (Fig. 9)
332 resulting in a stronger potential temperature gradient up to 400 m AGL compared to the IPM location. During the
333 day, the boundary layer height increases to 200–400 m above ground as indicated by the constant potential



334 temperature (e.g. Bauer et al., 2020) which is a typical value for European winter conditions (Seidel et al., 2012;
335 Wang et al., 2020). The PBL height estimates are confirmed by calculating the gradient Richardson number (Ri;
336 Chan, 2008) (not shown) which exceeds 0.25 at this altitude (Seidel et al., 2012; Lee and Wekker, 2016). After
337 sunset around 15:30 UTC the boundary layer collapses to a night-time stable boundary layer and a temperature
338 inversion occurs again.

339 4.2. Air quality

340 The most relevant air pollutants for air quality considerations in cities are NO₂ and PM₁₀. Sources for these are
341 mainly truck supply, transit, and commuter traffic through the city as well as advection from motorways south,
342 west, and northwest of Stuttgart. We start with the discussion of the simulated horizontal distributions followed
343 by vertical cross sections of NO₂ and PM₁₀.

344 4.2.1 Horizontal distribution

345 Figure 12 shows the horizontal distribution of the NO₂ concentration at the lowest model half level (~15 m AGL)
346 at the four timesteps 07:30 UTC, 12 UTC, 18 UTC and 23 UTC 21 January 2019.

347 At 7:30 UTC the morning traffic rush hour is visible in the NO₂ concentrations in Fig. 12a. High NO₂
348 concentrations of more than 80 µg m⁻³ are simulated along the motorway A81 in the northwest of the domain, over
349 the airport and over downtown Stuttgart. In the Neckar Valley the concentrations exceed 120 µg m⁻³. At noon time
350 (Fig. 12b), when turbulence is fully evolved (Fig. 11), the simulated NO₂ concentrations are less than 30 µg m⁻³
351 on average apparently due to vertical mixing of NO₂ (see next section). In the evening (Fig. 12c) the simulated
352 NO₂ concentrations increase again showing values of more than 100 µg m⁻³ over the airport and more than 150 µg
353 m⁻³ in downtown Stuttgart and the Neckar Valley due to road and air traffic. The high morning concentrations
354 along the northwestern motorway are not reached since the wind speed increases and the near surface winds turn
355 towards a westerly direction. According to the emission data set converted by the temporal factors, the evening
356 traffic spreads over a longer time. During the night (Fig. 12d), NO₂ accumulates in the Stuttgart basin as well as
357 the Neckar Valley due to the very low nocturnal boundary layer height of less than 200 m capped by an atmospheric
358 inversion (Fig. 11).

359 Apart from NO₂, the concentration PM₁₀ is an important parameter for air quality considerations and is the decisive
360 factor for proclaiming a “fine dust alarm” situation in Stuttgart (Stuttgart Municipality and German Meteorological
361 Service (DWD), 2019). Note that the simulated PM₁₀ concentrations include particles less than 2.5 µm of diameter
362 (PM_{2.5}) and that PM₁₀ is a diagnosed quantity in our model setup.

363 Figure 13 shows the horizontal distribution of PM₁₀ for the same time steps as shown in Fig 12.

364 During the morning traffic (Fig. 13a), PM₁₀ accumulates in the Stuttgart basin as this is an area with heavy traffic
365 during the morning and an atmospheric inversion is present (Fig. 7). Interestingly, the high NO₂ concentrations
366 along the motorway (Fig. 12a) do not lead to very high PM₁₀ concentrations potentially due to chemical transitions
367 caused by low temperatures.

368 During daytime when turbulence is fully evolved, the concentration of PM₁₀ decreases to less than 20 µg m⁻³ due
369 to vertical mixing and horizontal transport (see next section). After sunset (Fig. 13c) PM₁₀ starts to accumulate
370 again in the Stuttgart basin showing concentrations between 35–40 µg m⁻³. During the night (Fig. 13d) PM₁₀
371 accumulates over a large part of the model domain as the nocturnal boundary layer is very shallow, an inversion
372 layer is present 400 m AGL and the wind direction changes from north to west.



373 4.2.2 Vertical distribution of NO₂ and PM₁₀

374 In addition to the horizontal distribution of near surface NO₂ and PM₁₀, TP simulations with a fine vertical
375 resolution also enable qualitative insights into the vertical distribution of pollutants. Figure 14 shows West-East
376 cross sections at Neckartor (Fig. 1b) during the morning rush hour and at noon time. Neckartor is one of the
377 heaviest traffic locations in the Stuttgart city area.

378 The NO₂ concentration during the morning rush hour shows an accumulation along the motorway (red arrow in
379 Fig. 14a) and in the region around Neckartor (white arrow in Fig. 14a) with concentrations exceeding 100 µg m⁻³
380 as the atmospheric inversion prevents exchange with the layers above (Fig. 7). The vertical extent of concentrations
381 higher than 30 µg m⁻³ is about 200 m AGL with a strong reduction above.

382 During noon time (Fig. 14b), the simulated NO₂ concentration is much lower (less than 30 µg m⁻³) as turbulence
383 leads to a stronger mixing throughout the boundary layer up to 400 m AGL which is in accordance with the
384 simulated potential temperature timeseries shown in Fig. 11.

385 Figure 15a displays the simulated PM₁₀ concentrations during the morning rush hour. Similar like for NO₂, higher
386 concentrations of more than 25 µg m⁻³ is simulated along the motorway and in the Stuttgart basin. During the day,
387 PM₁₀ is vertically mixed showing a clear gradient around 800 m above sea level (ASL) (Fig. 15b) while
388 concentrations remain between 10-20 µg m⁻³ within the boundary layer.

389 Apart from the West-East cross sections it is also worthwhile to investigate the vertical temporal evolution of NO₂
390 and PM₁₀ concentrations. Therefore, Fig. 16 shows time height cross sections of NO₂ (top) and PM₁₀ (bottom) at
391 Neckartor as an example for a heavy traffic area in the basin.

392 Well visible are the high simulated NO₂ and PM₁₀ concentrations during the morning rush hour with peak values
393 of more than 120 µg m⁻³ NO₂ and more than 40 µg m⁻³ PM₁₀. The high concentrations of NO₂ and PM₁₀ are present
394 up to around 150-200 m AGL. During daytime, turbulence efficiently mixes the pollutants up to higher altitude
395 and the near surface concentrations are quickly reduced. During the evening when the very shallow boundary layer
396 has developed again and evening traffic commences, the particle concentrations increase, and peak values of more
397 than 30 µg m⁻³ are simulated below 100 m AGL.

398

399 5. Summary and conclusion

400 This paper describes the setup of a AQFS prototype using WRF-Chem for the Stuttgart Metropolitan area. Because
401 of the complex topography in this region, this simulation system requires a very high horizontal resolution down
402 to the turbulence permitting scale to represent all orographic and land cover features.

403 For the development of this prototype 21 January 2019 served as test case as this was a typical winter day with an
404 atmospheric inversion. In addition, this day was characterized as “fine dust alarm” situation where the PM₁₀
405 concentration at one of the heaviest traffic areas in the Stuttgart basin was expected to exceed 30 µg m⁻³. The
406 model setup encompassed three domains down to a turbulence permitting resolution of 50 m.

407 The initial conditions were provided by the ECMWF operational analysis, the CAMS reanalysis and WACCM
408 model for background chemistry. Emission data sets from CAMS-REG-AP and high-resolution data with 500 m
409 resolution from LUBW were combined to be used in the AQFS. As current emission data sets only provide annual
410 totals or means, a temporal decomposition following TNO was applied (Denier van der Gon et al., 2011).



411 For this case study, we focused on the results with respect to 2-m temperature, surface fluxes and boundary layer
412 evolution as well as horizontal and vertical distributions of NO₂ and PM₁₀.

413 Our results revealed that despite the complex topography in Stuttgart, the model is in general capable to simulate
414 a realistic diurnal cycle of 2-m temperatures although, compared to observations, differences of up to 1 K occur.
415 Apparently the model has difficulties with the dissolution of low stratus clouds between 03 and 06 UTC which
416 was also reported in the work of Steeneveld et al. (2015) resulting in a warm 2-m temperature bias during the
417 morning. Although no measurements are available, the surface sensible heat fluxes show a clear diurnal cycle with
418 the magnitude clearly depending on the underlying land cover type. The low simulated ground heat flux and its
419 fluctuations between 00 UTC and sunrise partially confirm the fog dissolution issue but more test cases are needed
420 for a more detailed investigation. Over grid cells where the single layer UCM is active, most of the ground heat
421 flux is stored in the canopy layer thus not transferred into the soil. The high vertical resolution of 100 levels enables
422 a realistic representation of the nocturnal and daytime temperature inversion with an accompanying shallow
423 boundary layer of less than 400 m during the day.

424 The simulation of PM₁₀ shows an exceedance of the 30 µg m⁻³ concentration threshold at the Neckartor station and
425 also fulfills the other fine dust alarm criteria shown in section 3. Compared to the usually unevenly distributed air
426 quality measurements, the AQFS allows further insights into the spatio-temporal pollutant distribution. The
427 horizontal distributions of NO₂ and PM₁₀ at this particular day clearly indicate the main polluted areas along the
428 motorways and in the Stuttgart basin. The special orography of Stuttgart with its basin favors the accumulation of
429 NO₂ and PM₁₀ in the morning and evening while the pollutants are well mixed to around 200-400 m AGL when
430 the boundary layer is fully evolved.

431 The simulation also shows that pollutants can be advected from the motorway A81 towards Stuttgart, depending
432 on the wind situation potentially leading to an increase of the NO₂ and PM₁₀ concentrations in the Stuttgart basin.
433 As can be seen from Figs. 12 and 13, the Neckar Valley can also have a large impact on the pollutant concentration
434 in the Stuttgart basin in case an atmospheric inversion together with prevailing easterly winds is present.

435 This is, to our knowledge, the first study of applying WRF-Chem on a TP resolution for an urban area. To derive
436 more robust conclusions with respect to air pollution, more cases studies with different weather situations during
437 winter and summer time are necessary. Nevertheless, our evaluation gives the following indications to further
438 improve the quality of such simulations:

- 439 I. Applying high spatial and temporal resolution gridded emission data from all pollution sources in near
440 real time to avoid extrapolating annual emissions to individual days.. This will help to enhance the
441 simulation of the diurnal cycles of chemical species.
- 442 II. Improving the chemical background e.g. by applying higher resolution products from the CAMS
443 European Air quality project (Marécal et al., 2015). This will help to have a more detailed structure of
444 the chemical constituents beneficial for further downscaling simulations.
- 445 III. Using a longer spin-up period and applying a larger TP model domain to further improve the spin-up of
446 turbulence in the model
- 447 IV. Considering vertical distribution of surface emissions (e.g. Bieser et al., 2011; Guevara et al., 2020)
- 448 V. Considerably increase the number of pollutant measurements to allow more robust conclusions



449 The AQFS has a great potential for urban planning applications. For example, land cover could be changed from
450 urban low density to urban high density to investigate the impact of urban re-densification e.g. on temperature and
451 air quality. Although no BEP can be applied on the TP resolution with our combination of parameterizations,
452 changes of the parameters required for the single layer UCM offer the opportunity to perform sensitivity analysis
453 with respect to different building heights, urban greening effects (Fallmann et al., 2016), or anthropogenic heat
454 (Karlický et al., 2020).

455 Although air quality modeling on the TP scale is a very challenging and computationally expensive task, we are
456 convinced that the AQFS will have a great potential to further improve process understanding and will certainly
457 help politicians to make decisions on a more scientifically valid basis.

458 **Code and data availability**

459 The WRF-Chem code version 4.0.3 can be downloaded from [https://github.com/wrf-](https://github.com/wrf-model/WRF/archive/v4.0.3.tar.gz)
460 [model/WRF/archive/v4.0.3.tar.gz](https://github.com/wrf-model/WRF/archive/v4.0.3.tar.gz). ECMWF analysis data can be obtained from [https://apps.ecmwf.int/archive-](https://apps.ecmwf.int/archive-catalogue/?type=an&class=od&stream=oper&expver=1)
461 [catalogue/?type=an&class=od&stream=oper&expver=1](https://apps.ecmwf.int/archive-catalogue/?type=an&class=od&stream=oper&expver=1) (last access: 26 August 2020). The user's affiliation needs
462 to belong to an ECMWF member state to benefit from these data sets. Due to restrictions on the input data sets for
463 this simulation, the data can only be made available upon special request from the corresponding author.

464 **Author Contributions**

465 TS prepared all emission data, set up the model and performed the simulation supported by HSB. HSB reclassified
466 the CORINE land use data set. KWS and TB conceived the idea and coordinated the project with VW. TS prepared
467 all figures and wrote the manuscript with input from all authors. All authors equally contributed to the scientific
468 discussion and helped to shape the research.

469 **Competing interests**

470 The authors declare that they have no conflict of interest.

471 **Acknowledgements**

472 This study has been performed within the EU-funded project *Open Forecast* (Action number 2017-DE-IA-0170).
473 We acknowledge ECMWF for providing analysis data from the operational IFS and CAMS reanalysis. The
474 Emissions of atmospheric Compounds and Compilation of Ancillary Data (ECCAD) system is acknowledged for
475 providing the CAMS-REG-AP Emission data set. We acknowledge the use of the WRF-Chem preprocessor tool
476 MOZBC, provided by the Atmospheric Chemistry Observations and Modeling Lab (ACOM) of NCAR. The
477 Baden-Württemberg State Institute for the Environment (LUBW) is highly acknowledged for providing high-
478 resolution annual emission data and for the high-resolution land cover data. Joachim Ingwersen from the
479 Department of Biogeophysics at the University of Hohenheim is acknowledged for converting the soil texture data.
480 Joachim Fallmann from the University of Mainz is acknowledged for providing the necessary code enhancement
481 of the dry deposition driver module to correctly couple the urban canopy model. The simulation was performed
482 on the national supercomputer Cray XC40 Hazel Hen at the High Performance Computing Center Stuttgart
483 (HLRS) within the WRFSCALE project..

484 **References**



- 485 Ackermann, I. J., Hass, H., Memmesheimer, M., Ebel, A., Binkowski, F. S., and Shankar, U.:
486 Modal aerosol dynamics model for Europe, *Atmospheric Environment*, 32, 2981–2999,
487 [https://doi.org/10.1016/S1352-2310\(98\)00006-5](https://doi.org/10.1016/S1352-2310(98)00006-5), 1998.
- 488 Baldauf, M., Seifert, A., Förstner, J., Majewski, D., Raschendorfer, M., and Reinhardt, T.:
489 Operational Convective-Scale Numerical Weather Prediction with the COSMO Model:
490 Description and Sensitivities, *Mon. Wea. Rev.*, 139, 3887–3905,
491 <https://doi.org/10.1175/MWR-D-10-05013.1>, 2011.
- 492 Barker, D., Huang, X.-Y., Liu, Z., Auligné, T., Zhang, X., Rugg, S., Ajjaji, R., Bourgeois, A., Bray,
493 J., Chen, Y., Demirtas, M., Guo, Y.-R., Henderson, T., Huang, W., Lin, H.-C., Michalakes, J.,
494 Rizvi, S., and Zhang, X.: The Weather Research and Forecasting Model's Community
495 Variational/Ensemble Data Assimilation System: WRFDA, *Bull. Amer. Meteor. Soc.*, 93,
496 831–843, <https://doi.org/10.1175/BAMS-D-11-00167.1>, 2012.
- 497 Bauer, H.-S., Muppa, S. K., Wulfmeyer, V., Behrendt, A., Warrach-Sagi, K., and Späth, F.:
498 Multi-nested WRF simulations for studying planetary boundary layer processes on the
499 turbulence-permitting scale in a realistic mesoscale environment, *Tellus A: Dynamic
500 Meteorology and Oceanography*, 72, 1–28,
501 <https://doi.org/10.1080/16000870.2020.1761740>, 2020.
- 502 Bieser, J., Aulinger, A., Matthias, V., Quante, M., and van der Denier Gon, H. A. C.: Vertical
503 emission profiles for Europe based on plume rise calculations, *Environmental pollution
504 (Barking, Essex 1987)*, 159, 2935–2946, <https://doi.org/10.1016/j.envpol.2011.04.030>,
505 2011.
- 506 Bonavita, M., Hólm, E., Isaksen, L., and Fisher, M.: The evolution of the ECMWF hybrid data
507 assimilation system, *Q.J.R. Meteorol. Soc.*, 142, 287–303,
508 <https://doi.org/10.1002/qj.2652>, 2016.
- 509 Brasseur, G. P., Hauglustaine, D. A., Walters, S., Rasch, P. J., Müller, J.-F., Granier, C., and Tie,
510 X. X.: MOZART, a global chemical transport model for ozone and related chemical tracers:
511 1. Model description, *J. Geophys. Res.*, 103, 28265–28289,
512 <https://doi.org/10.1029/98JD02397>, 1998.
- 513 Butcher, G., Barnes, C., and Owen, L.: Landsat: The cornerstone of global land imaging, *GIM
514 International*, January/February 2019, 31–35, available at:
515 <http://pubs.er.usgs.gov/publication/70202363>, 2019.
- 516 Chan, P. W.: Determination of Richardson number profile from remote sensing data and its
517 aviation application, *IOP Conf. Ser.: Earth Environ. Sci.*, 1, 12043,
518 <https://doi.org/10.1088/1755-1315/1/1/012043>, 2008.
- 519 Chen, D., Liu, Z., Ban, J., Zhao, P., and Chen, M.: Retrospective analysis of 2015–2017
520 wintertime PM_{2.5} in China: response to emission regulations and the role of meteorology,
521 *Atmos. Chem. Phys.*, 19, 7409–7427, <https://doi.org/10.5194/acp-19-7409-2019>, 2019.
- 522 Copernicus: Copernicus official website, <https://atmosphere.copernicus.eu/>, last access: 21
523 July 2020.
- 524 Coppola, E., Sobolowski, S., Pichelli, E., Raffaele, F., Ahrens, B., Anders, I., Ban, N., Bastin, S.,
525 Belda, M., Belusic, D., Caldas-Alvarez, A., Cardoso, R. M., Davolio, S., Dobler, A.,
526 Fernandez, J., Fita, L., Fumiere, Q., Giorgi, F., Goergen, K., Güttler, I., Halenka, T.,
527 Heinzeller, D., Hodnebrog, Ø., Jacob, D., Kartsios, S., Katragkou, E., Kendon, E., Khodayar,
528 S., Kunstmann, H., Knist, S., Lavín-Gullón, A., Lind, P., Lorenz, T., Maraun, D., Marelle, L.,



- 529 van Meijgaard, E., Milovac, J., Myhre, G., Panitz, H.-J., Piazza, M., Raffa, M., Raub, T.,
530 Rockel, B., Schär, C., Sieck, K., Soares, P. M. M., Somot, S., Srncic, L., Stocchi, P., Tölle, M.
531 H., Truhetz, H., Vautard, R., Vries, H. de, and Warrach-Sagi, K.: A first-of-its-kind multi-
532 model convection permitting ensemble for investigating convective phenomena over
533 Europe and the Mediterranean, *Clim Dyn*, 55, 3–34, [https://doi.org/10.1007/s00382-018-](https://doi.org/10.1007/s00382-018-4521-8)
534 4521-8, 2020.
- 535 Corsmeier, U., Kalthoff, N., Barthlott, C., Aoshima, F., Behrendt, A., Di Girolamo, P.,
536 Doringner, M., Handwerker, J., Kottmeier, C., Mahlke, H., Mobbs, S. D., Norton, E. G.,
537 Wickert, J., and Wulfmeyer, V.: Processes driving deep convection over complex terrain:
538 a multi-scale analysis of observations from COPS IOP 9c, *Q.J.R. Meteorol. Soc.*, 137, 137–
539 155, <https://doi.org/10.1002/qj.754>, 2011.
- 540 Danielson, J. J. and Gesch, D. B.: Global multi-resolution terrain elevation data 2010
541 (GMTED2010), Open-File report, 2011.
- 542 Denier van der Gon, H., Hendriks, C., Kuenen, J., Segers, A., and Visschedijk, A.: Description
543 of current temporal emission patterns and sensitivity of predicted AQ for temporal
544 emission patterns: EU FP7 MACC deliverable report D_D-EMIS_1.3, TNO report, 2011.
- 545 European Union: Copernicus Land Monitoring Service 2017, European Environment Agency,
546 2017.
- 547 European Union: Copernicus Land Monitoring Service 2012, European Environment Agency,
548 2012.
- 549 Fallmann, J.: Numerical simulations to assess the effect of urban heat island mitigation
550 strategies on regional air quality, PhD Thesis, Universität zu Köln, Cologne, 2014.
- 551 Fallmann, J., Forkel, R., and Emeis, S.: Secondary effects of urban heat island mitigation
552 measures on air quality, *Atmospheric Environment*, 125, 199–211,
553 <https://doi.org/10.1016/j.atmosenv.2015.10.094>, 2016.
- 554 Fallmann, J., Emeis, S., and Suppan, P.: Mitigation of urban heat stress – a modelling case
555 study for the area of Stuttgart, *DIE ERDE – Journal of the Geographical Society of Berlin*,
556 144, 202–216, <https://doi.org/10.12854/erde-144-15>, 2014.
- 557 Farr, T. G., Rosen, P. A., Caro, E., Crippen, R., Duren, R., Hensley, S., Kobrick, M., Paller, M.,
558 Rodriguez, E., Roth, L., Seal, D., Shaffer, S., Shimada, J., Umland, J., Werner, M., Oskin,
559 M., Burbank, D., and Alsdorf, D.: The Shuttle Radar Topography Mission, *Rev. Geophys.*,
560 45, <https://doi.org/10.1029/2005RG000183>, 2007.
- 561 Flemming, J., Huijnen, V., Arteta, J., Bechtold, P., Beljaars, A., Blechschmidt, A.-M.,
562 Diamantakis, M., Engelen, R. J., Gaudel, A., Inness, A., Jones, L., Josse, B., Katragkou, E.,
563 Marecal, V., Peuch, V.-H., Richter, A., Schultz, M. G., Stein, O., and Tsikerdekis, A.:
564 Tropospheric chemistry in the Integrated Forecasting System of ECMWF, *Geosci. Model*
565 *Dev.*, 8, 975–1003, <https://doi.org/10.5194/gmd-8-975-2015>, 2015.
- 566 Forkel, R., Balzarini, A., Baró, R., Bianconi, R., Curci, G., Jiménez-Guerrero, P., Hirtl, M.,
567 Honzak, L., Lorenz, C., Im, U., Pérez, J. L., Pirovano, G., San José, R., Tuccella, P., Werhahn,
568 J., and Žabkar, R.: Analysis of the WRF-Chem contributions to AQMEII phase2 with
569 respect to aerosol radiative feedbacks on meteorology and pollutant distributions,
570 *Atmospheric Environment*, 115, 630–645,
571 <https://doi.org/10.1016/j.atmosenv.2014.10.056>, 2015.



- 572 Freitas, S. R., Longo, K. M., Alonso, M. F., Pirre, M., Marecal, V., Grell, G., Stockler, R., Mello,
573 R. F., and Sánchez Gácita, M.: PREP-CHEM-SRC – 1.0: a preprocessor of trace gas and
574 aerosol emission fields for regional and global atmospheric chemistry models, *Geosci.*
575 *Model Dev.*, 4, 419–433, <https://doi.org/10.5194/gmd-4-419-2011>, 2011.
- 576 Freitas, S. R., Panetta, J., Longo, K. M., Rodrigues, L. F., Moreira, D. S., Rosário, N. E., Silva
577 Dias, P. L., Silva Dias, M. A. F., Souza, E. P., Freitas, E. D., Longo, M., Frassoni, A., Fazenda,
578 A. L., Santos e Silva, C. M., Pavani, C. A. B., Eiras, D., França, D. A., Massaru, D., Silva, F. B.,
579 Santos, F. C., Pereira, G., Camponogara, G., Ferrada, G. A., Campos Velho, H. F., Menezes,
580 I., Freire, J. L., Alonso, M. F., Gácita, M. S., Zazur, M., Fonseca, R. M., Lima, R. S., Siqueira,
581 R. A., Braz, R., Tomita, S., Oliveira, V., and Martins, L. D.: The Brazilian developments on
582 the Regional Atmospheric Modeling System (BRAMS 5.2): an integrated environmental
583 model tuned for tropical areas, *Geosci. Model Dev.*, 10, 189–222,
584 <https://doi.org/10.5194/gmd-10-189-2017>, 2017.
- 585 García-Díez, M., Lauwaet, D., Hooyberghs, H., Ballester, J., Ridder, K. de, and Rodó, X.:
586 Advantages of using a fast urban boundary layer model as compared to a full mesoscale
587 model to simulate the urban heat island of Barcelona, *Geosci. Model Dev.*, 9, 4439–4450,
588 <https://doi.org/10.5194/gmd-9-4439-2016>, 2016.
- 589 Giorgi, F., Coppola, E., Solmon, F., Mariotti, L., Sylla, M. B., Bi, X., Elguindi, N., Diro, G. T.,
590 Nair, V., Giuliani, G., Turuncoglu, U. U., Cozzini, S., Güttler, I., O’Brien, T. A., Tawfik, A. B.,
591 Shalaby, A., Zakey, A. S., Steiner, A. L., Stordal, F., Sloan, L. C., and Brankovic, C.: RegCM4:
592 model description and preliminary tests over multiple CORDEX domains, *Clim. Res.*, 52,
593 7–29, <https://doi.org/10.3354/cr01018>, 2012.
- 594 Granier, C., Darras, S., Denier van der Gon, H., Doubalova, J., Elguindi, N., Galle, B., Gauss,
595 M., Guevara, M., Jalkanen, J.-P., Kuenen, J., Liousse, C., Quack, B., Simpson, D., and
596 Sindelarova, K.: The Copernicus Atmosphere Monitoring Service global and regional
597 emissions (April 2019 version), 2019.
- 598 Grell, G. A., Peckham, S. E., Schmitz, R., McKeen, S. A., Frost, G., Skamarock, W. C., and Eder,
599 B.: Fully coupled “online” chemistry within the WRF model, *Atmospheric Environment*,
600 39, 6957–6975, <https://doi.org/10.1016/j.atmosenv.2005.04.027>, 2005.
- 601 Guevara, M., Jorba, O., Tena, C., van der Denier Gon, H., Kuenen, J., Elguindi-Solmon, N.,
602 Darras, S., Granier, C., and Pérez García-Pando, C.: CAMS-TEMPO: global and European
603 emission temporal profile maps for atmospheric chemistry modelling, 2020.
- 604 Heinze, R., Moseley, C., Böske, L. N., Muppa, S. K., Maurer, V., Raasch, S., and Stevens, B.:
605 Evaluation of large-eddy simulations forced with mesoscale model output for a multi-
606 week period during a measurement campaign, *Atmos. Chem. Phys.*, 17, 7083–7109,
607 <https://doi.org/10.5194/acp-17-7083-2017>, 2017a.
- 608 Heinze, R., Dipankar, A., Henken, C. C., Moseley, C., Sourdeval, O., Trömel, S., Xie, X.,
609 Adamidis, P., Ament, F., Baars, H., Barthlott, C., Behrendt, A., Blahak, U., Bley, S., Brdar,
610 S., Brueck, M., Crewell, S., Deneke, H., Di Girolamo, P., Evaristo, R., Fischer, J., Frank, C.,
611 Friederichs, P., Göcke, T., Gorges, K., Hande, L., Hanke, M., Hansen, A., Hege, H.-C.,
612 Hoose, C., Jahns, T., Kalthoff, N., Klocke, D., Kneifel, S., Knippertz, P., Kuhn, A., van Laar,
613 T., Macke, A., Maurer, V., Mayer, B., Meyer, C. I., Muppa, S. K., Neggens, R. A. J., Orlandi,
614 E., Pantillon, F., Pospichal, B., Röber, N., Scheck, L., Seifert, A., Seifert, P., Senf, F., Siligam,
615 P., Simmer, C., Steinke, S., Stevens, B., Wapler, K., Weniger, M., Wulfmeyer, V., Zängl, G.,



- 616 Zhang, D., and Quaas, J.: Large-eddy simulations over Germany using ICON: a
617 comprehensive evaluation, *Q.J.R. Meteorol. Soc.*, **143**, 69–100,
618 <https://doi.org/10.1002/qj.2947>, 2017b.
- 619 Hengl, T., Heuvelink, G. B. M., Kempen, B., Leenaars, J. G. B., Walsh, M. G., Shepherd, K. D.,
620 Sila, A., MacMillan, R. A., Mendes de Jesus, J., Tamene, L., and Tondoh, J. E.: Mapping Soil
621 Properties of Africa at 250 m Resolution: Random Forests Significantly Improve Current
622 Predictions, *PloS one*, **10**, e0125814, <https://doi.org/10.1371/journal.pone.0125814>,
623 2015.
- 624 Hengl, T., Jesus, J. M. de, MacMillan, R. A., Batjes, N. H., Heuvelink, G. B. M., Ribeiro, E.,
625 Samuel-Rosa, A., Kempen, B., Leenaars, J. G. B., Walsh, M. G., and Gonzalez, M. R.:
626 SoilGrids1km--global soil information based on automated mapping, *PloS one*, **9**,
627 e105992, <https://doi.org/10.1371/journal.pone.0105992>, 2014.
- 628 Hong, S.-Y., Noh, Y., and Dudhia, J.: A New Vertical Diffusion Package with an Explicit
629 Treatment of Entrainment Processes, *Mon. Wea. Rev.*, **134**, 2318–2341,
630 <https://doi.org/10.1175/MWR3199.1>, 2006.
- 631 Horowitz, L. W., Walters, S., Mauzerall, D. L., Emmons, L. K., Rasch, P. J., Granier, C., Tie, X.,
632 Lamarque, J.-F., Schultz, M. G., Tyndall, G. S., Orlando, J. J., and Brasseur, G. P.: A global
633 simulation of tropospheric ozone and related tracers: Description and evaluation of
634 MOZART, version 2, *J. Geophys. Res.*, **108**, n/a-n/a,
635 <https://doi.org/10.1029/2002JD002853>, 2003.
- 636 Huszar, P., Karlický, J., Ďoubalová, J., Šindelářová, K., Nováková, T., Belda, M., Halenka, T.,
637 Žák, M., and Pišoft, P.: Urban canopy meteorological forcing and its impact on ozone and
638 PM_{2.5}: role of vertical turbulent transport, *Atmos. Chem. Phys.*, **20**, 1977–2016,
639 <https://doi.org/10.5194/acp-20-1977-2020>, 2020.
- 640 Iacono, M. J., Delamere, J. S., Mlawer, E. J., Shephard, M. W., Clough, S. A., and Collins, W.
641 D.: Radiative forcing by long-lived greenhouse gases: Calculations with the AER radiative
642 transfer models, *J. Geophys. Res.*, **113**, <https://doi.org/10.1029/2008JD009944>, 2008.
- 643 Inness, A., Ades, M., Agustí-Panareda, A., Barré, J., Benedictow, A., Blechschmidt, A.-M.,
644 Dominguez, J. J., Engelen, R., Eskes, H., Flemming, J., Huijnen, V., Jones, L., Kipling, Z.,
645 Massart, S., Parrington, M., Peuch, V.-H., Razinger, M., Remy, S., Schulz, M., and Suttie,
646 M.: The CAMS reanalysis of atmospheric composition, *Atmos. Chem. Phys.*, **19**, 3515–
647 3556, <https://doi.org/10.5194/acp-19-3515-2019>, 2019.
- 648 Jiménez, P. A., Dudhia, J., González-Rouco, J. F., Navarro, J., Montávez, J. P., and García-
649 Bustamante, E.: A Revised Scheme for the WRF Surface Layer Formulation, *Mon. Wea.*
650 *Rev.*, **140**, 898–918, <https://doi.org/10.1175/MWR-D-11-00056.1>, 2012.
- 651 Jin, L., Li, Z., He, Q., Miao, Q., Zhang, H., and Yang, X.: Observation and simulation of near-
652 surface wind and its variation with topography in Urumqi, West China, *J Meteorol Res*,
653 **30**, 961–982, <https://doi.org/10.1007/s13351-016-6012-3>, 2016.
- 654 Karlický, J., Huszár, P., Nováková, T., Belda, M., Švábík, F., Ďoubalová, J., and Halenka, T.: The
655 'urban meteorology island': a multi-model ensemble analysis, 2020.
- 656 Kawabata, T., Schwitalla, T., Adachi, A., Bauer, H.-S., Wulfmeyer, V., Nagumo, N., and
657 Yamauchi, H.: Observational operators for dual polarimetric radars in variational data
658 assimilation systems (PolRad VAR v1.0), *Geosci. Model Dev.*, **11**, 2493–2501,
659 <https://doi.org/10.5194/gmd-11-2493-2018>, 2018.



- 660 Kealy, J. C., Efstathiou, G. A., and Beare, R. J.: The Onset of Resolved Boundary-Layer
661 Turbulence at Grey-Zone Resolutions, *Boundary-Layer Meteorol.*, **171**, 31–52,
662 <https://doi.org/10.1007/s10546-018-0420-0>, 2019.
- 663 Khan, B., Banzhaf, S., Chan, E. C., Forkel, R., Kanani-Sühring, F., Ketelsen, K., Kurppa, M.,
664 Maronga, B., Mauder, M., Raasch, S., Russo, E., Schaap, M., and Sühring, M.:
665 Development of an atmospheric chemistry model coupled to the PALM model system
666 6.0: Implementation and first applications, *Geosci. Model Dev.*,
667 <https://doi.org/10.5194/gmd-2020-286>, 2020, under review.
- 668 Kosovic, B.: Subgrid-scale modelling for the large-eddy simulation of high-Reynolds-number
669 boundary layers, *J. Fluid Mech.*, **336**, 151–182,
670 <https://doi.org/10.1017/S0022112096004697>, 1997.
- 671 Kuenen, J. J. P., Visschedijk, A. J. H., Jozwicka, M., and van der Denier Gon, H. A. C.: TNO-
672 MACC-II emission inventory; a multi-year (2003–2009) consistent high-resolution
673 European emission inventory for air quality modelling, *Atmos. Chem. Phys.*, **14**, 10963–
674 10976, <https://doi.org/10.5194/acp-14-10963-2014>, 2014.
- 675 Kuik, F., Kerschbaumer, A., Lauer, A., Lupascu, A., Schneidemesser, E. von, and Butler, T. M.:
676 Top-down quantification of NO_x emissions from traffic in an urban area using a high-
677 resolution regional atmospheric chemistry model, *Atmos. Chem. Phys.*, **18**, 8203–8225,
678 <https://doi.org/10.5194/acp-18-8203-2018>, 2018.
- 679 Kuik, F., Lauer, A., Churkina, G., van der Denier Gon, H. A. C., Fenner, D., Mar, K. A., and
680 Butler, T. M.: Air quality modelling in the Berlin–Brandenburg region using WRF-Chem
681 v3.7.1: sensitivity to resolution of model grid and input data, *Geosci. Model Dev.*, **9**,
682 4339–4363, <https://doi.org/10.5194/gmd-9-4339-2016>, 2016.
- 683 Kusaka, H. and Kimura, F.: Coupling a Single-Layer Urban Canopy Model with a Simple
684 Atmospheric Model: Impact on Urban Heat Island Simulation for an Idealized Case, *JMSJ*,
685 **82**, 67–80, <https://doi.org/10.2151/jmsj.82.67>, 2004.
- 686 Lee, T. R. and Wekker, S. F. J. de: Estimating Daytime Planetary Boundary Layer Heights over
687 a Valley from Rawinsonde Observations at a Nearby Airport: An Application to the Page
688 Valley in Virginia, United States, *J. Appl. Meteor. Climatol.*, **55**, 791–809,
689 <https://doi.org/10.1175/JAMC-D-15-0300.1>, 2016.
- 690 Li, Z., Zhou, Y., Wan, B., Chung, H., Huang, B., and Liu, B.: Model evaluation of high-
691 resolution urban climate simulations: using the WRF/Noah LSM/SLUCM model (Version
692 3.7.1) as a case study, *Geosci. Model Dev.*, **12**, 4571–4584, <https://doi.org/10.5194/gmd-12-4571-2019>, 2019.
- 694 Mailler, S., Menut, L., Khvorostyanov, D., Valari, M., Couvidat, F., Siour, G., Turquety, S.,
695 Briant, R., Tuccella, P., Bessagnet, B., Colette, A., Létinois, L., Markakis, K., and Meleux, F.:
696 CHIMERE-2017: from urban to hemispheric chemistry-transport modeling, *Geosci. Model*
697 *Dev.*, **10**, 2397–2423, <https://doi.org/10.5194/gmd-10-2397-2017>, 2017.
- 698 Manders, A. M. M., Bultjes, P. J. H., Curier, L., van der Denier Gon, H. A. C., Hendriks, C.,
699 Jonkers, S., Kranenburg, R., Kuenen, J. J. P., Segers, A. J., Timmermans, R. M. A.,
700 Visschedijk, A. J. H., Wichink Kruit, R. J., van Pul, W. A. J., Sauter, F. J., van der Swaluw, E.,
701 Swart, D. P. J., Douros, J., Eskes, H., van Meijgaard, E., van Ulft, B., van Velthoven, P.,
702 Banzhaf, S., Mues, A. C., Stern, R., Fu, G., Lu, S., Heemink, A., van Velzen, N., and Schaap,



- 703 M.: Curriculum vitae of the LOTOS–EUROS (v2.0) chemistry transport model, *Geosci.*
704 *Model Dev.*, 10, 4145–4173, <https://doi.org/10.5194/gmd-10-4145-2017>, 2017.
- 705 Mar, K. A., Ojha, N., Pozzer, A., and Butler, T. M.: Ozone air quality simulations with WRF-
706 Chem (v3.5.1) over Europe: model evaluation and chemical mechanism comparison,
707 *Geosci. Model Dev.*, 9, 3699–3728, <https://doi.org/10.5194/gmd-9-3699-2016>, 2016.
- 708 Marécal, V., Peuch, V.-H., Andersson, C., Andersson, S., Arteta, J., Beekmann, M.,
709 Benedictow, A., Bergström, R., Bessagnet, B., Cansado, A., Chéroux, F., Colette, A.,
710 Coman, A., Curier, R. L., van der Denier Gon, H. A. C., Drouin, A., Elbern, H., Emili, E.,
711 Engelen, R. J., Eskes, H. J., Foret, G., Friese, E., Gauss, M., Giannaros, C., Guth, J., Joly, M.,
712 Jaumouillé, E., Josse, B., Kadygrov, N., Kaiser, J. W., Krajsek, K., Kuenen, J., Kumar, U.,
713 Liora, N., Lopez, E., Malherbe, L., Martinez, I., Melas, D., Meleux, F., Menut, L., Moinat,
714 P., Morales, T., Parmentier, J., Piacentini, A., Plu, M., Poupkou, A., Queguiner, S.,
715 Robertson, L., Rouil, L., Schaap, M., Segers, A., Sofiev, M., Tarasson, L., Thomas, M.,
716 Timmermans, R., Valdebenito, Á., van Velthoven, P., van Versendaal, R., Vira, J., and Ung,
717 A.: A regional air quality forecasting system over Europe: the MACC-II daily ensemble
718 production, *Geosci. Model Dev.*, 8, 2777–2813, [https://doi.org/10.5194/gmd-8-2777-](https://doi.org/10.5194/gmd-8-2777-2015)
719 2015, 2015.
- 720 Maronga, B., Gryschka, M., Heinze, R., Hoffmann, F., Kanani-Sühring, F., Keck, M., Ketelsen,
721 K., Letzel, M. O., Sühring, M., and Raasch, S.: The Parallelized Large-Eddy Simulation
722 Model (PALM) version 4.0 for atmospheric and oceanic flows: model formulation, recent
723 developments, and future perspectives, *Geosci. Model Dev.*, 8, 2515–2551,
724 <https://doi.org/10.5194/gmd-8-2515-2015>, 2015.
- 725 Maronga, B., Banzhaf, S., Burmeister, C., Esch, T., Forkel, R., Fröhlich, D., Fuka, V., Gehrke, K.
726 F., Geletič, J., Giersch, S., Gronemeier, T., Groß, G., Heldens, W., Hellsten, A., Hoffmann,
727 F., Inagaki, A., Kadasch, E., Kanani-Sühring, F., Ketelsen, K., Khan, B. A., Knigge, C., Knoop,
728 H., Krč, P., Kurppa, M., Maamari, H., Matzarakis, A., Mauder, M., Pallasch, M., Pavlik, D.,
729 Pfafferott, J., Resler, J., Rissmann, S., Russo, E., Salim, M., Schrempf, M., Schwenkel, J.,
730 Seckmeyer, G., Schubert, S., Sühring, M., Tils, R. von, Vollmer, L., Ward, S., Witha, B.,
731 Wurps, H., Zeidler, J., and Raasch, S.: Overview of the PALM model system 6.0, *Geosci.*
732 *Model Dev.*, 13, 1335–1372, <https://doi.org/10.5194/gmd-13-1335-2020>, 2020.
- 733 Maronga, B., Gross, G., Raasch, S., Banzhaf, S., Forkel, R., Heldens, W., Kanani-Sühring, F.,
734 Matzarakis, A., Mauder, M., Pavlik, D., Pfafferott, J., Schubert, S., Seckmeyer, G., Sieker,
735 H., and Winderlich, K.: Development of a new urban climate model based on the model
736 PALM – Project overview, planned work, and first achievements, *metz*, 28, 105–119,
737 <https://doi.org/10.1127/metz/2019/0909>, 2019.
- 738 Marsh, D. R., Mills, M. J., Kinnison, D. E., Lamarque, J.-F., Calvo, N., and Polvani, L. M.:
739 Climate Change from 1850 to 2005 Simulated in CESM1(WACCM), *J. Climate*, 26, 7372–
740 7391, <https://doi.org/10.1175/JCLI-D-12-00558.1>, 2013.
- 741 Martilli, A., Clappier, A., and Rotach, M. W.: An Urban Surface Exchange Parameterisation for
742 Mesoscale Models, *Boundary-Layer Meteorology*, 104, 261–304,
743 <https://doi.org/10.1023/A:1016099921195>, 2002.
- 744 Maynard, R., Krzyzanowski, M., Vilahur, N., and Héroux, M.-E.: Evolution of WHO air quality
745 guidelines: Past, present and future, WHO Regional Office for Europe, Copenhagen, 32
746 pp., 2017.



- 747 Memmesheimer, M., Friese, E., Ebel, A., Jakobs, H. J., Feldmann, H., Kessler, C., and Piekorz,
748 G.: Long-term simulations of particulate matter in Europe on different scales using
749 sequential nesting of a regional model, *IJEP*, 22, 108,
750 <https://doi.org/10.1504/IJEP.2004.005530>, 2004.
- 751 Nakayama, H., Takemi, T., and Nagai, H.: Large-eddy simulation of urban boundary-layer
752 flows by generating turbulent inflows from mesoscale meteorological simulations,
753 *Atmosph. Sci. Lett.*, 13, 180–186, <https://doi.org/10.1002/asl.377>, 2012.
- 754 Niu, G.-Y., Yang, Z.-L., Mitchell, K. E., Chen, F., Ek, M. B., Barlage, M., Kumar, A., Manning, K.,
755 Niyogi, D., Rosero, E., Tewari, M., and Xia, Y.: The community Noah land surface model
756 with multiparameterization options (Noah-MP): 1. Model description and evaluation with
757 local-scale measurements, *J. Geophys. Res.*, 116, <https://doi.org/10.1029/2010JD015139>,
758 2011.
- 759 Panosetti, D., Böing, S., Schlemmer, L., and Schmidli, J.: Idealized Large-Eddy and Convection-
760 Resolving Simulations of Moist Convection over Mountainous Terrain, *J. Atmos. Sci.*, 73,
761 4021–4041, <https://doi.org/10.1175/JAS-D-15-0341.1>, 2016.
- 762 Pfister, G. G., Parrish, D. D., Worden, H., Emmons, L. K., Edwards, D. P., Wiedinmyer, C.,
763 Diskin, G. S., Huey, G., Oltmans, S. J., Thouret, V., Weinheimer, A., and Wisthaler, A.:
764 Characterizing summertime chemical boundary conditions for airmasses entering the US
765 West Coast, *Atmos. Chem. Phys.*, 11, 1769–1790, [https://doi.org/10.5194/acp-11-1769-](https://doi.org/10.5194/acp-11-1769-2011)
766 2011, 2011.
- 767 Prein, A. F., Langhans, W., Fosser, G., Ferrone, A., Ban, N., Goergen, K., Keller, M., Tölle, M.,
768 Gutjahr, O., Feser, F., Brisson, E., Kollet, S., Schmidli, J., van Lipzig, N. P. M., and Leung, R.:
769 A review on regional convection-permitting climate modeling: Demonstrations,
770 prospects, and challenges, *Rev. Geophys.*, 53, 323–361,
771 <https://doi.org/10.1002/2014RG000475>, 2015.
- 772 Resler, J., Eben, K., Geletič, J., Krč, P., Rosecký, M., Sührling, M., Belda, M., Fuka, V., Halenka,
773 T., Huszár, P., Karlický, J., Benešová, N., Ďoubalová, J., Honzáková, K., Keder, J.,
774 Nápravníková, Š., and Vlček, O.: Validation of the PALM model system 6.0 in real urban
775 environment; case study of Prague-Dejvice, Czech Republic, *Geosci. Model Dev.*,
776 <https://doi.org/10.5194/gmd-2020-175>, 2020, under review.
- 777 Rieger, D., Bangert, M., Bischoff-Gauss, I., Förstner, J., Lundgren, K., Reinert, D., Schröter, J.,
778 Vogel, H., Zängl, G., Ruhnke, R., and Vogel, B.: ICON–ART 1.0 – a new online-coupled
779 model system from the global to regional scale, *Geosci. Model Dev.*, 8, 1659–1676,
780 <https://doi.org/10.5194/gmd-8-1659-2015>, 2015.
- 781 Salamanca, F. and Martilli, A.: A new Building Energy Model coupled with an Urban Canopy
782 Parameterization for urban climate simulations—part II. Validation with one dimension
783 off-line simulations, *Theor Appl Climatol*, 99, 345–356, [https://doi.org/10.1007/s00704-](https://doi.org/10.1007/s00704-009-0143-8)
784 009-0143-8, 2010.
- 785 Schell, B., Ackermann, I. J., Hass, H., Binkowski, F. S., and Ebel, A.: Modeling the formation of
786 secondary organic aerosol within a comprehensive air quality model system, *J. Geophys.*
787 *Res.*, 106, 28275–28293, <https://doi.org/10.1029/2001JD000384>, 2001.
- 788 Scherer, D., Antretter, F., Bender, S., Cortekar, J., Emeis, S., Fehrenbach, U., Gross, G., Halbig,
789 G., Hasse, J., Maronga, B., Raasch, S., and Scherber, K.: Urban Climate Under Change
790 [UC]2 – A National Research Programme for Developing a Building-Resolving



- 791 Atmospheric Model for Entire City Regions, *metz*, 28, 95–104,
792 <https://doi.org/10.1127/metz/2019/0913>, 2019.
- 793 Seidel, D. J., Zhang, Y., Beljaars, A., Golaz, J.-C., Jacobson, A. R., and Medeiros, B.:
794 Climatology of the planetary boundary layer over the continental United States and
795 Europe, *J. Geophys. Res.*, 117, n/a-n/a, <https://doi.org/10.1029/2012JD018143>, 2012.
- 796 Skamarock, W. C., Klemp, J. B., Dudhia, J., Gill, D. O., Liu, Z., Berner, J., Wang, W., Powers, J.
797 G., Duda, M. G., Barker, D. M., and Huang, X.-Y.: A Description of the Advanced Research
798 WRF Model Version 4, 2019.
- 799 Steeneveld, G. J., Ronda, R. J., and Holtslag, A. A. M.: The Challenge of Forecasting the Onset
800 and Development of Radiation Fog Using Mesoscale Atmospheric Models, *Boundary-*
801 *Layer Meteorol.*, 154, 265–289, <https://doi.org/10.1007/s10546-014-9973-8>, 2015.
- 802 Stockwell, W. R., Middleton, P., Chang, J. S., and Tang, X.: The second generation regional
803 acid deposition model chemical mechanism for regional air quality modeling, *J. Geophys.*
804 *Res.*, 95, 16343, <https://doi.org/10.1029/JD095iD10p16343>, 1990.
- 805 Stuttgart Municipality and German Meteorological Service (DWD): Requirements for fine
806 dust situations, <https://feinstaubalarm.stuttgart.de/img/mdb/item/584405/119353.pdf>,
807 last access: 20 August 2020, 2019.
- 808 Sun, W., Liu, Z., Chen, D., Zhao, P., and Chen, M.: Development and application of the
809 WRFDA-Chem three-dimensional variational (3DVAR) system: aiming to improve air
810 quality forecasting and diagnose model deficiencies, *Atmos. Chem. Phys.*, 20, 9311–9329,
811 <https://doi.org/10.5194/acp-20-9311-2020>, 2020.
- 812 Teixeira, J. C., Fallmann, J., Carvalho, A. C., and Rocha, A.: Surface to boundary layer coupling
813 in the urban area of Lisbon comparing different urban canopy models in WRF, *Urban*
814 *Climate*, 28, 100454, <https://doi.org/10.1016/j.uclim.2019.100454>, 2019.
- 815 Thompson, G., Field, P. R., Rasmussen, R. M., and Hall, W. D.: Explicit Forecasts of Winter
816 Precipitation Using an Improved Bulk Microphysics Scheme. Part II: Implementation of a
817 New Snow Parameterization, *Mon. Wea. Rev.*, 136, 5095–5115,
818 <https://doi.org/10.1175/2008MWR2387.1>, 2008.
- 819 Thundathil, R., Schwitalla, T., Behrendt, A., Muppa, S. K., ADAM, S., and Wulfmeyer, V.:
820 Assimilation of Lidar Water Vapour Mixing Ratio and Temperature Profiles into a
821 Convection-Permitting Model, *JMSJ*, <https://doi.org/10.2151/jmsj.2020-049>, 2020.
- 822 Thunis, P., Degraeuwe, B., Pisoni, E., Trombetti, M., Peduzzi, E., Belis, C. A., Wilson, J., and
823 Vignati, E.: Urban PM_{2.5} atlas: Air quality in European cities, JRC science for policy report,
824 28804, Publications Office, Luxembourg, 1 online resource, 2017.
- 825 UN: The World's Cities in 2018, United Nations, 2018.
- 826 Valcke, S., Balaji, V., Craig, A., DeLuca, C., Dunlap, R., Ford, R. W., Jacob, R., Larson, J.,
827 O'Kuinghtons, R., Riley, G. D., and Vertenstein, M.: Coupling technologies for Earth
828 System Modelling, *Geosci. Model Dev.*, 5, 1589–1596, [https://doi.org/10.5194/gmd-5-](https://doi.org/10.5194/gmd-5-1589-2012)
829 [1589-2012](https://doi.org/10.5194/gmd-5-1589-2012), 2012.
- 830 Vogel, B., Vogel, H., Bäumer, D., Bangert, M., Lundgren, K., Rinke, R., and Stanelle, T.: The
831 comprehensive model system COSMO-ART – Radiative impact of aerosol on the state of
832 the atmosphere on the regional scale, *Atmos. Chem. Phys.*, 9, 8661–8680,
833 <https://doi.org/10.5194/acp-9-8661-2009>, 2009.



- 834 Wang, D., Stachlewska, I. S., Song, X., Heese, B., and Nemuc, A.: Variability of the Boundary
835 Layer Over an Urban Continental Site Based on 10 Years of Active Remote Sensing
836 Observations in Warsaw, *Remote Sensing*, 12, 340, <https://doi.org/10.3390/rs12020340>,
837 2020.
- 838 WHO: WHO Air quality guidelines for particulate matter, ozone, nitrogen dioxide and sulfur
839 dioxide. Global update 2005., 2005.
- 840 Yang, Z.-L., Niu, G.-Y., Mitchell, K. E., Chen, F., Ek, M. B., Barlage, M., Longuevergne, L.,
841 Manning, K., Niyogi, D., Tewari, M., and Xia, Y.: The community Noah land surface model
842 with multiparameterization options (Noah-MP): 2. Evaluation over global river basins, *J.*
843 *Geophys. Res.*, 116, <https://doi.org/10.1029/2010JD015140>, 2011.
- 844 Zängl, G., Reinert, D., Rípodas, P., and Baldauf, M.: The ICON (ICOsahedral Non-hydrostatic)
845 modelling framework of DWD and MPI-M: Description of the non-hydrostatic dynamical
846 core, *Q.J.R. Meteorol. Soc.*, 141, 563–579, <https://doi.org/10.1002/qj.2378>, 2015.
- 847 Zhang, X., Huang, X.-Y., Liu, J., Poterjoy, J., Weng, Y., Zhang, F., and Wang, H.: Development
848 of an Efficient Regional Four-Dimensional Variational Data Assimilation System for WRF,
849 *Journal of Atmospheric and Oceanic Technology*, 31, 2777–2794,
850 <https://doi.org/10.1175/JTECH-D-13-00076.1>, 2014.
- 851 Zhong, M., Saikawa, E., Liu, Y., Naik, V., Horowitz, L. W., Takigawa, M., Zhao, Y., Lin, N.-H.,
852 and Stone, E. A.: Air quality modeling with WRF-Chem v3.5 in East Asia: sensitivity to
853 emissions and evaluation of simulated air quality, *Geosci. Model Dev.*, 9, 1201–1218,
854 <https://doi.org/10.5194/gmd-9-1201-2016>, 2016.
- 855 Zieliński, M., Fortuniak, K., Pawlak, W., and Siedlecki, M.: Long-term Turbulent Sensible-
856 Heat-Flux Measurements with a Large-Aperture Scintillometer in the Centre of Łódź,
857 Central Poland, *Boundary-Layer Meteorol.*, 167, 469–492,
858 <https://doi.org/10.1007/s10546-017-0331-5>, 2018.
859
- 860

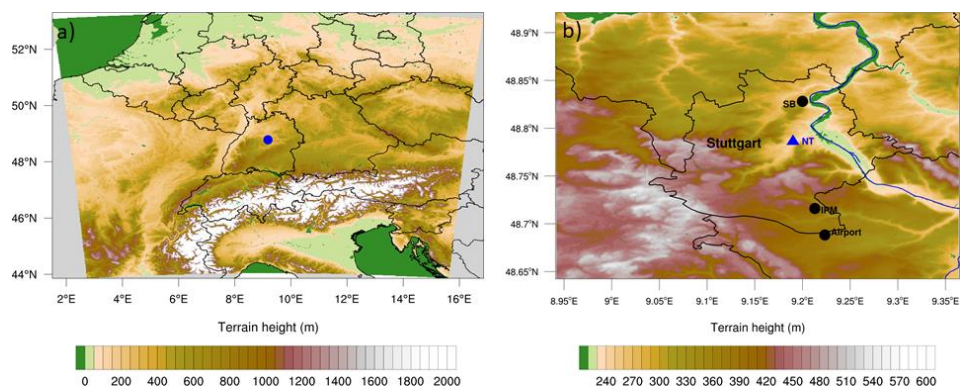


Figure 1: Model domain 1 (a) and domain 3 (b). The blue dot in (a) denotes Stuttgart. Black dots in (b) show the location of the meteorological measurement sites. The blue diamond in (b) denotes the Neckartor (NT) location and the blue contour line denotes the Neckar River (River data © OpenStreetMap contributors 2020. Distributed under a Creative Commons BY-SA License).

861

862

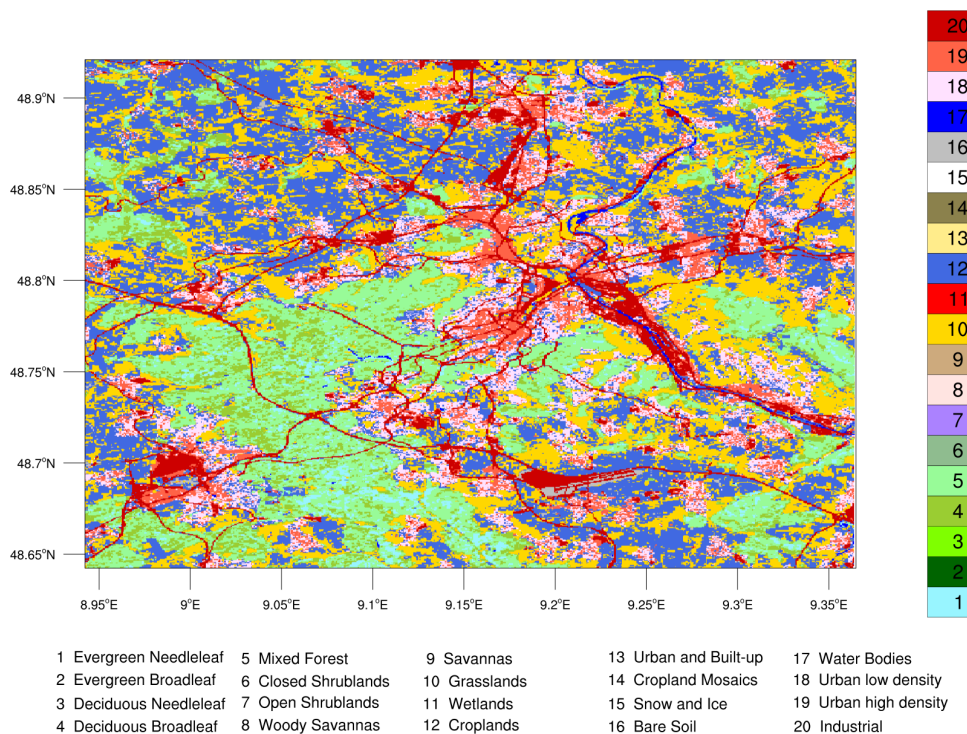


Figure 2: Land cover data from the Baden-Württemberg State Institute for the Environment, Survey and Nature Conservation (LUBW) reclassified for WRF in the innermost domain at a resolution of 50 m.

863

864

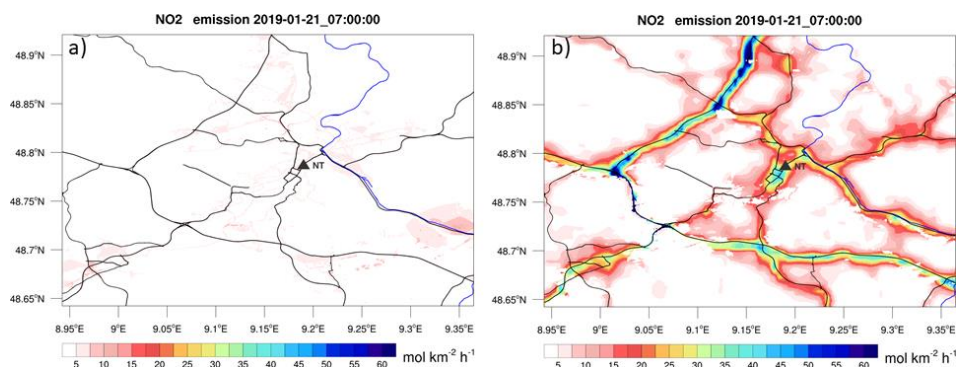


Figure 3: NO₂ emissions valid at 07 UTC on January 21, 2019. (a) shows the emissions derived from the CAMS-REG-AP data set and (b) shows the emissions derived from the BW-EMISS data set (Map Data © OpenStreetMap contributors 2020. Distributed under a Creative Commons BY-SA License).

865

866

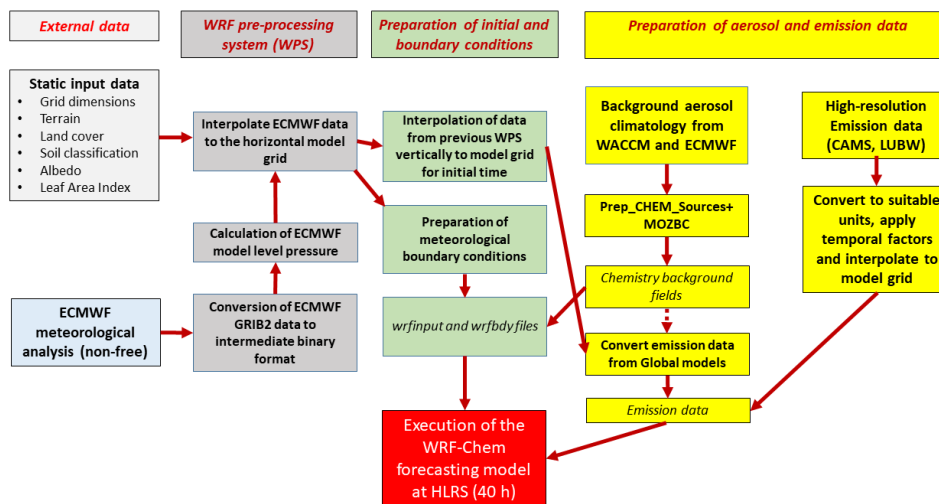


Figure 4: Workflow of the AQFS prototype system.

867

868

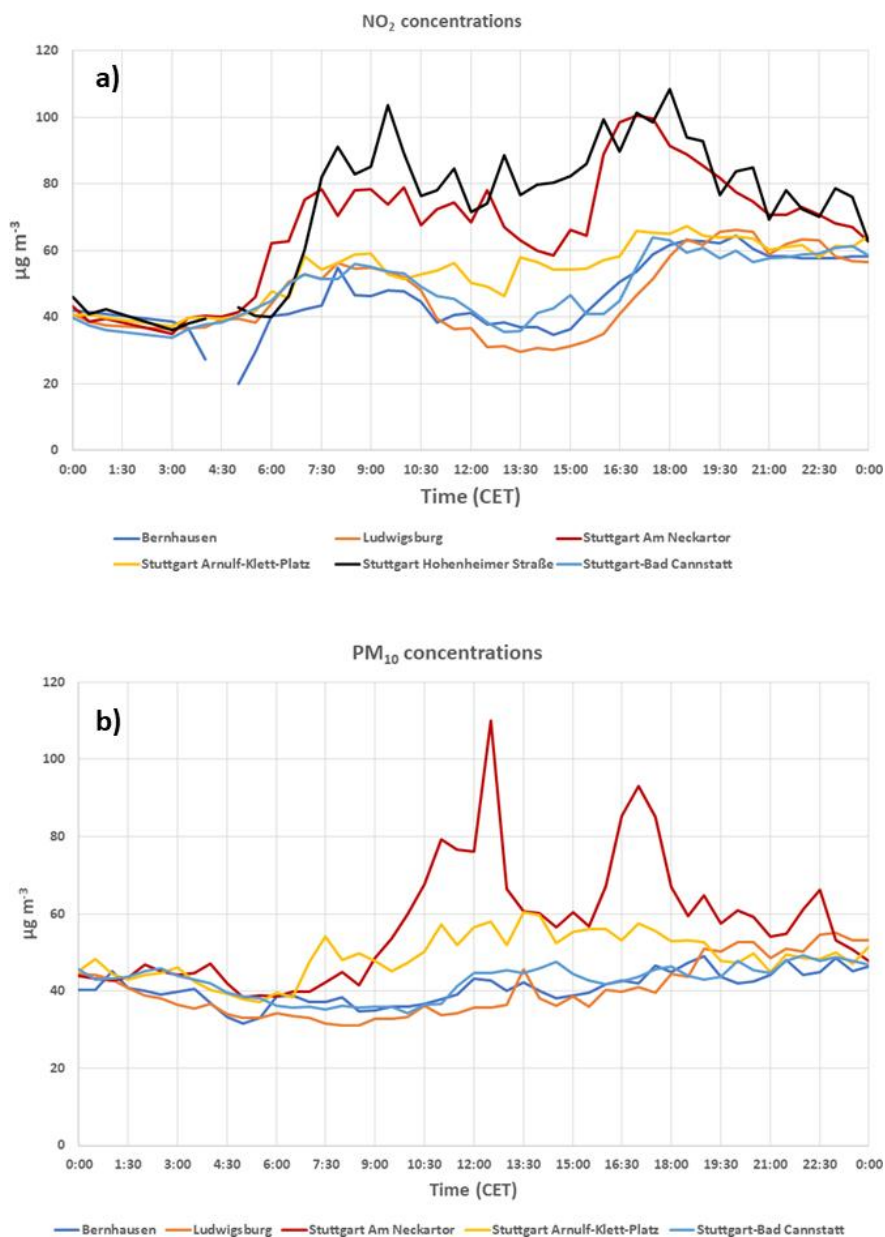


Figure 5: Observed NO_2 (a) and PM_{10} (b) concentrations at several stations distributed over the model domain on 21 January 2019. The time zone (CET) corresponds to local time. Measurements at Neckartor, Hohenheimer Strasse, and Arnulf-Klett Platz are directly taken next to the main road.

869

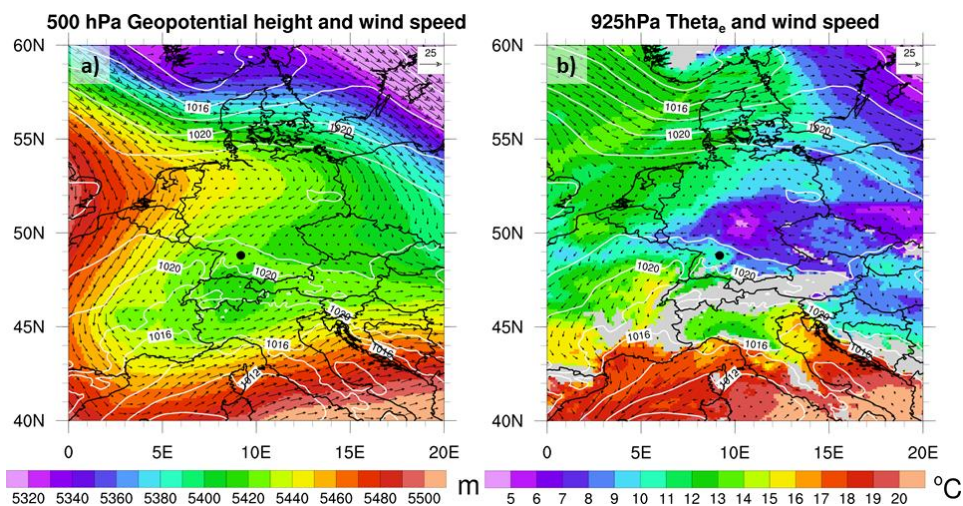


Figure 6: (a) ECMWF operational analysis of 500 hPa geopotential height, sea level pressure (white contour lines) together with 500 hPa wind velocities valid at 00 UTC 21 January 2019. (b) shows the 925hPa equivalent potential temperature together with 925 hPa wind velocities and sea level pressure (white contour lines). Gray areas indicate values below the ECMWF model terrain. The black dot denotes Stuttgart and the reference wind vector length (top right corner of each Figure)) is equal to 25 m s^{-1} .

870

871

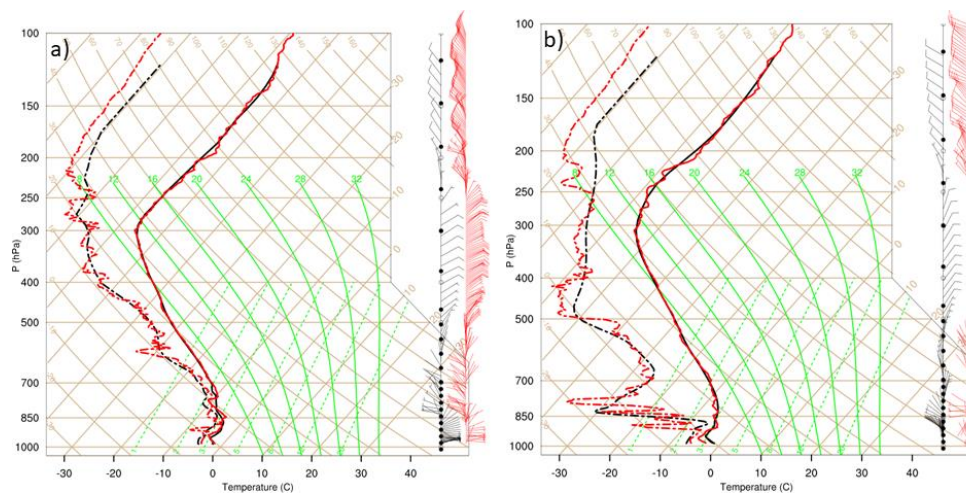


Figure 7: Comparison of temperature, dewpoint and wind of the WRF model simulation (black line) and the sounding from Stuttgart-Schnarrenberg (red line) valid at 00 UTC (a) and 11 UTC (b) 21 January 2019. The solid lines denote the temperature profile and the dash-dotted line denotes the dewpoint profile. Wind barbs denote wind speed in m s^{-1} .

872

873

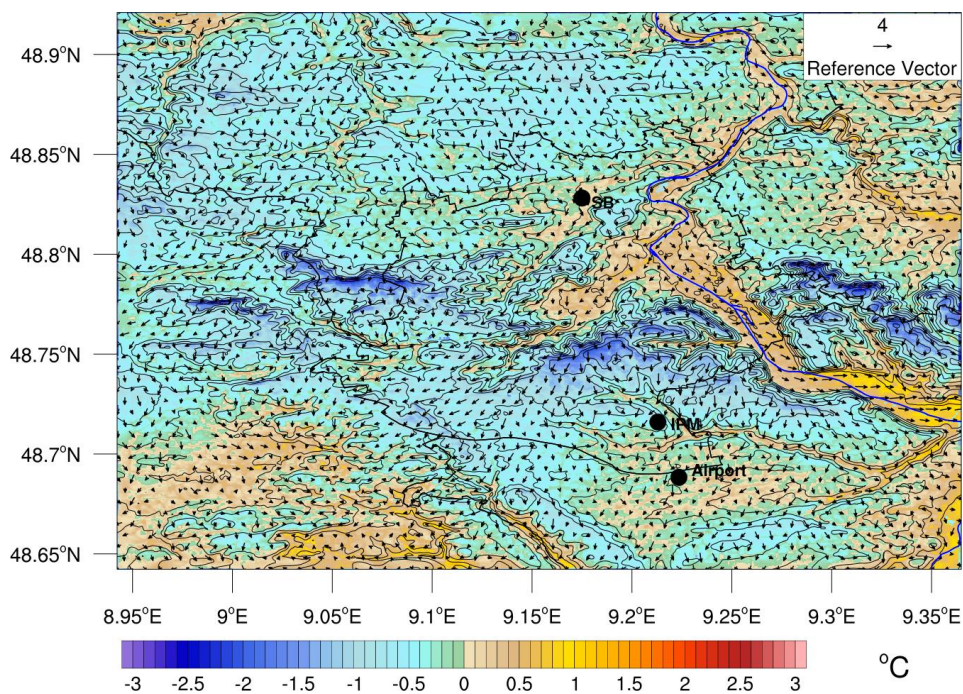


Figure 8: 2-m temperature together with 10-m wind velocities at 12 UTC 21 January 2019. The thick black line denotes the Stuttgart city limits and the thin black contour lines denote the terrain. The blue line denotes the Neckar River (River data © OpenStreetMap contributors 2020. Distributed under a Creative Commons BY-SA License).

874

875

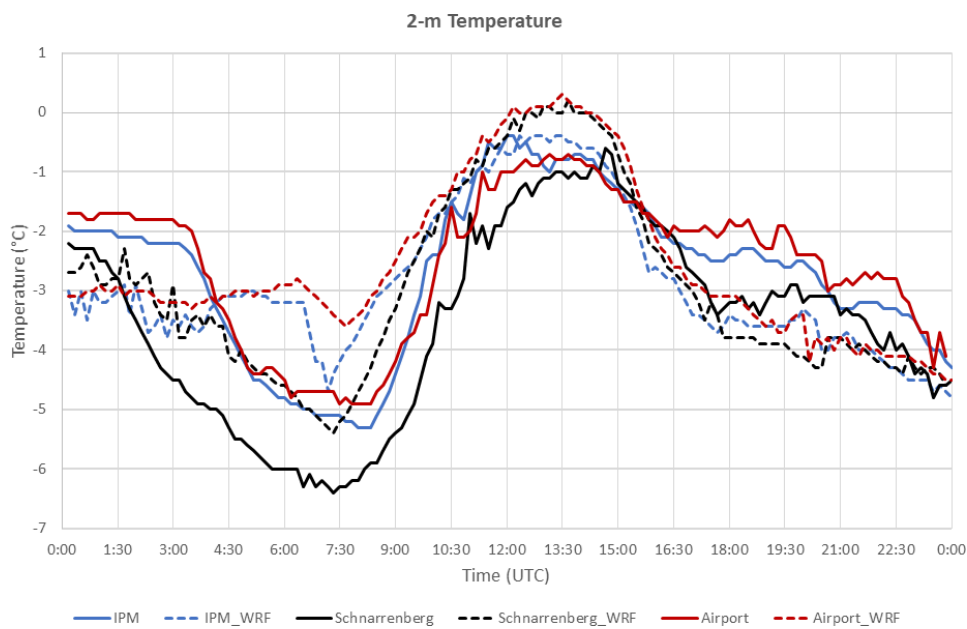


Figure 9: Diurnal cycle of 2-m temperatures for the three meteorological stations shown in Fig. 3. Solid lines denote the observation, dashed lines denote the model simulation. The temporal resolution is 10 minutes.

876

877

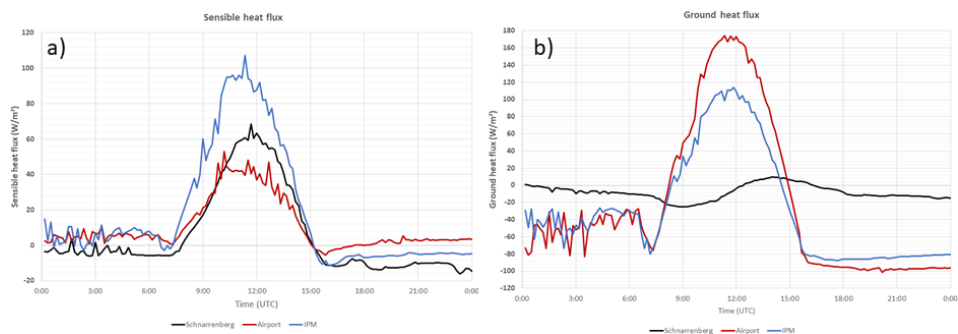


Figure 10: Diurnal cycle of simulated sensible heat flux (SH, a) and ground heat flux (GRDFLX, b) at the three meteorological stations (white dots in Fig. 3). Positive values of GRDFLX indicate fluxes into the soil. The land cover categories are bare soil (airport), croplands (IPM), and urban (Schnarrenberg).

878

879

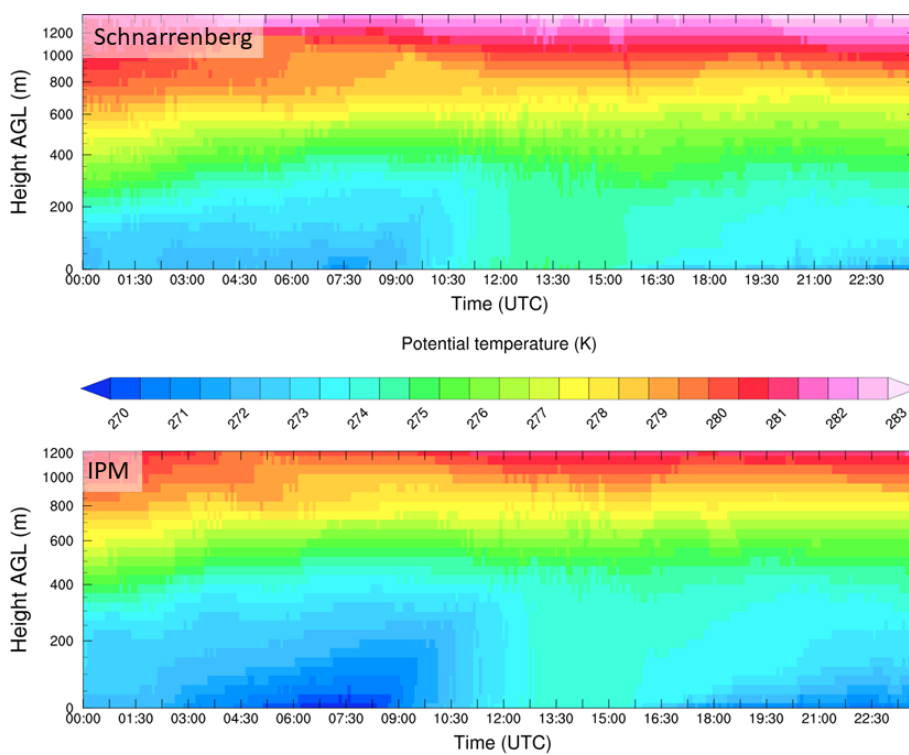


Figure 11: Time-height cross section of the simulated potential temperature at IPM (top) and Schnarrenberg (bottom). The displayed altitude is above ground level (AGL).

880

881

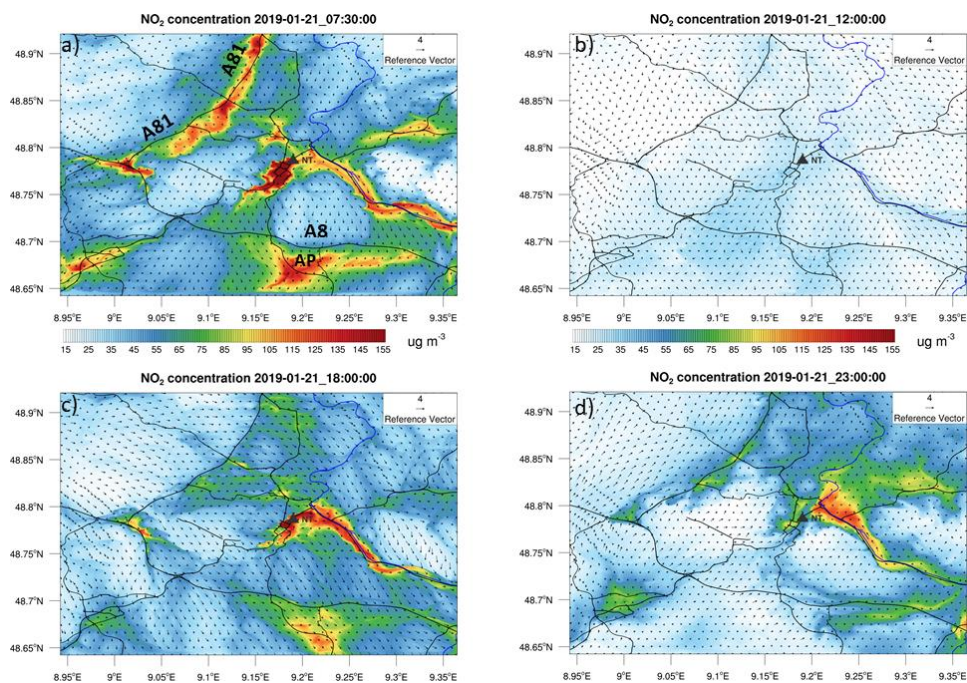


Figure 12: NO₂ concentration at the lowest model level for 07:30 UTC, 12 UTC, 18:00 UTC, and 23 UTC (from a to d) 21 January 2019. The black contour lines denote main roads and motorways in and around Stuttgart (Map Data © OpenStreetMap contributors 2020. Distributed under a Creative Commons BY-SA License). AP denotes the airport, A8 and A81 denote the main motorways around Stuttgart.

882

883

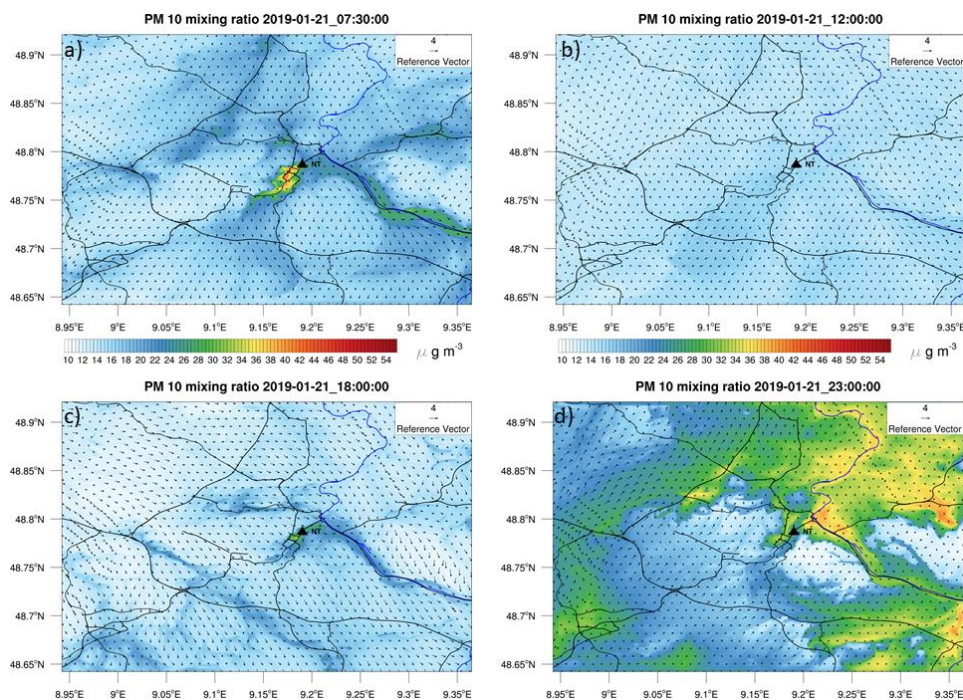


Figure 13: Same as Fig. 12 but for PM₁₀ (Map Data © OpenStreetMap contributors 2020. Distributed under a Creative Commons BY-SA License).

884

885

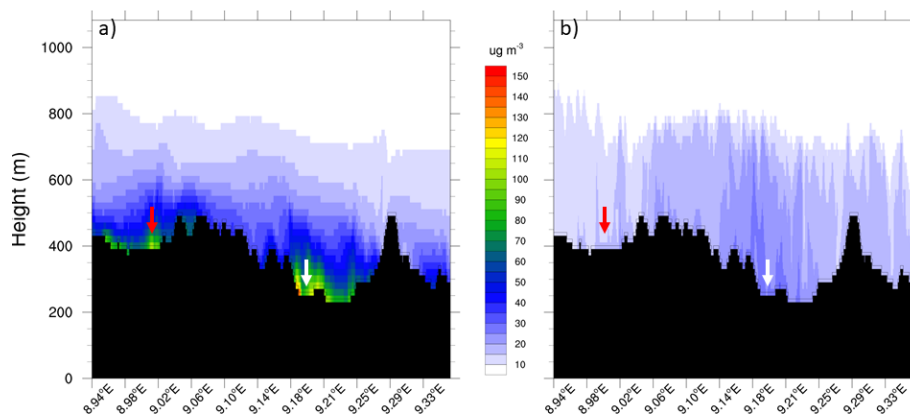


Figure 14: West-East cross section through Neckartor displaying the NO₂ concentration at 07:30 UTC (a) and 12 UTC (b), 21 January 2019. The red arrow denotes the motorway A81 and the white arrow denotes the Neckartor location. The black area shows the model terrain above mean sea level.

886

887

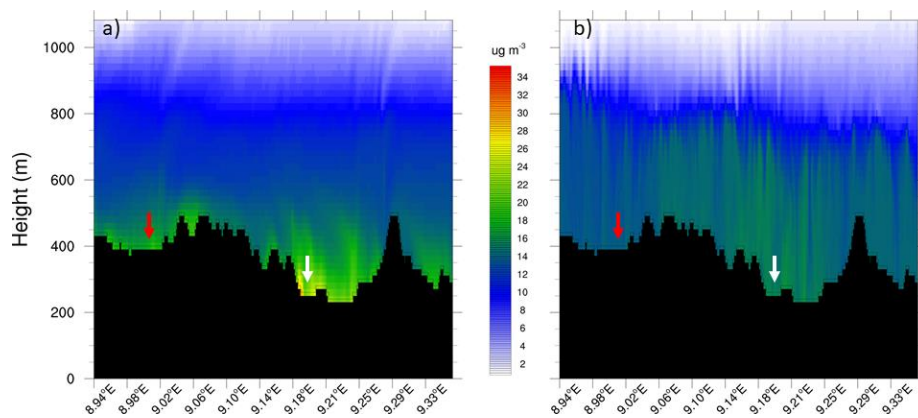


Figure 15: Same as Fig. 14 but for PM₁₀.

888

889

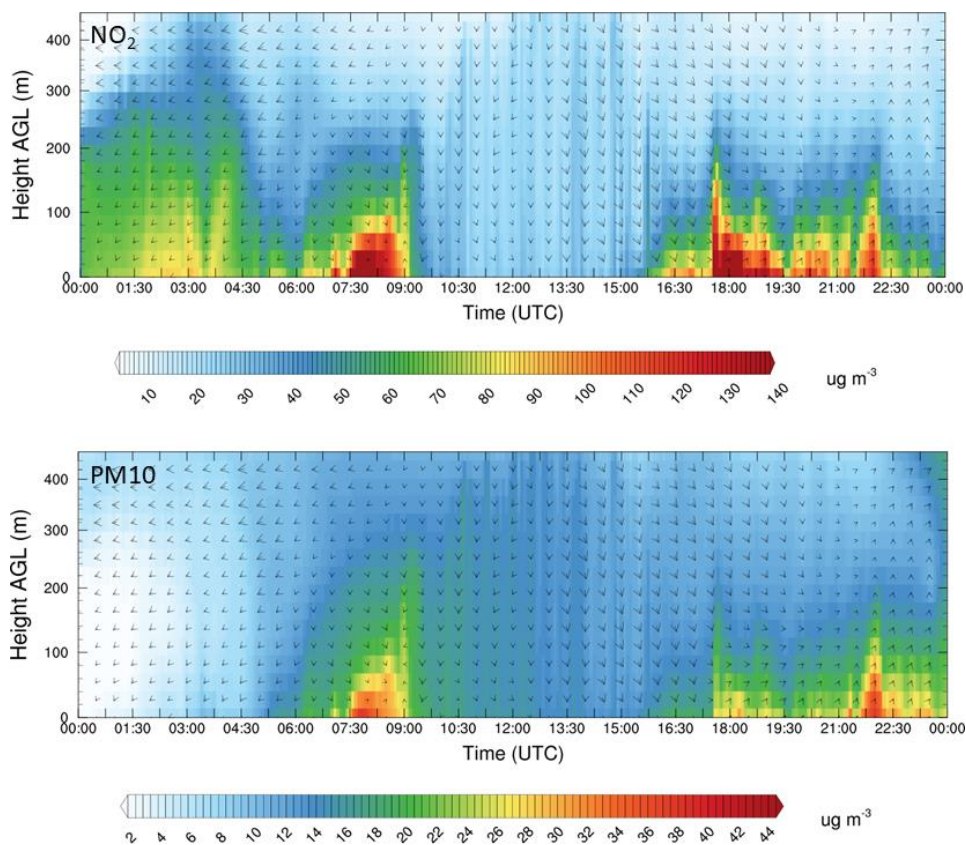


Fig. 16: Time height cross section of NO₂ (top) and PM₁₀ (bottom) at Neckartor (NT) up to an altitude of 450 m AGL.

890